

MICROCOPY

CHART

2

NRL Memorandum Report 5762

# Numerical Simulation of the Laser-Target Interaction and Blast Wave Formation in the DNA/NRL Laser Experiment

JOHN L. GIULIANI, JR. AND MARGARET MULBRANDON

*Geophysical and Plasma Dynamics Branch  
Plasma Physics Division*

May 9, 1986

This research was sponsored by the Defense Nuclear Agency under Subtask W99QMXWA,  
work unit 00010 and work unit title "Plasma Structure Evolution."



NAVAL RESEARCH LABORATORY  
Washington, D.C.

DTIC  
ELECTE  
MAY 15 1986  
S E D

Approved for public release, distribution unlimited

86 5

AD-A167 119

DTIC FILE COPY

## **DISCLAIMER NOTICE**

**THIS DOCUMENT IS BEST QUALITY PRACTICABLE. THE COPY FURNISHED TO DTIC CONTAINED A SIGNIFICANT NUMBER OF PAGES WHICH DO NOT REPRODUCE LEGIBLY.**

AD-A167119

SECURITY CLASSIFICATION OF THIS PAGE

REPORT DOCUMENTATION PAGE

1a. REPORT SECURITY CLASSIFICATION UNCLASSIFIED		1b. RESTRICTIVE MARKINGS	
2a. SECURITY CLASSIFICATION AUTHORITY		3. DISTRIBUTION / AVAILABILITY OF REPORT	
2b. DECLASSIFICATION / DOWNGRADING SCHEDULE		Approved for public release; distribution unlimited.	
4. PERFORMING ORGANIZATION REPORT NUMBER(S) NRL Memorandum Report 5762		5. MONITORING ORGANIZATION REPORT NUMBER(S)	
6a. NAME OF PERFORMING ORGANIZATION Naval Research Laboratory	6b. OFFICE SYMBOL (if applicable) Code 4780	7a. NAME OF MONITORING ORGANIZATION	
6c. ADDRESS (City, State, and ZIP Code) Washington, DC 20375-5000		7b. ADDRESS (City, State, and ZIP Code)	
8a. NAME OF FUNDING / SPONSORING ORGANIZATION Defense Nuclear Agency	8b. OFFICE SYMBOL (if applicable) RAAE	9. PROCUREMENT INSTRUMENT IDENTIFICATION NUMBER	
8c. ADDRESS (City, State, and ZIP Code) Washington, DC 20305		10. SOURCE OF FUNDING NUMBERS	
		PROGRAM ELEMENT NO 63223C	PROJECT NO TASK NO. WORK UNIT ACCESSION NO BR010-43
11. TITLE (Include Security Classification) Numerical Simulation of the Laser-Target Interaction and Blast Wave Formation in the DNA/NRL Laser Experiment			
12. PERSONAL AUTHOR(S) Guiliani, John L., Jr. and Mulbrandon, Margaret			
13a. TYPE OF REPORT Interim	13b. TIME COVERED FROM TO	14. DATE OF REPORT (Year, Month, Day) 1986 May 9	15. PAGE COUNT 60
16. SUPPLEMENTARY NOTATION This research was sponsored by the Defense Nuclear Agency under Subtask W99QMXWA, work unit 00010 and work unit title "Plasma Structure Evolution."			
17. COSATI CODES		18. SUBJECT TERMS (Continue on reverse if necessary and identify by block number)	
FIELD	GROUP	SUB-GROUP	Laser plasmas, Numerical simulation Blast wave, Raleigh-Taylor instability
19. ABSTRACT (Continue on reverse if necessary and identify by block number)			
<p>A numerical simulation of the ablation of a planar, aluminum foil target by a neodymium laser in the presence of a 2.5 Torr nitrogen background gas is presented. The simulation includes inverse bremsstrahlung absorption during the laser pulse, the cold isotherm in the equation of state for solid aluminum, non-equilibrium chemistry for both the target material and the background gas, radiation transport of the continuum, ion and electron energy equations, and blast wave formation in the background gas. The simulation is followed out to &gt; 50 nsec from the peak of the laser pulse. Although the Lagrangian code is 1-D, the divergence of the ablated target material expanding toward the laser (forward) as well as the rearward acceleration of the remaining target is accounted for by using an oblate spheroidal coordinate system.</p> <p>The primary results of the simulations are as follows: (i), by ~ 50 nsec a cavity with <math>T_e \sim 60</math> eV and <math>n_e \sim 2 \times 10^{17}</math> <math>\text{cm}^{-3}</math> has formed behind the denser and cooler forward moving blast wave; (ii), this cavity is not in chemical equilibrium but highly overionized for its temperature with predominantly <math>\text{Al}^{+9}</math>, <math>\text{Al}^{+10}</math>, <math>\text{Al}^{+11}</math>, <math>\text{N}^{+5}</math> and <math>\text{N}^{+6}</math>; and (iii), the conditions for a deceleration driven Rayleigh-Taylor instability are satisfied at the rear blast wave near one equal mass radius. This last feature may account for the experimentally observed flocculi on the rearward side.</p>			
20. DISTRIBUTION / AVAILABILITY OF ABSTRACT <input checked="" type="checkbox"/> UNCLASSIFIED/UNLIMITED <input type="checkbox"/> SAME AS RPT. <input type="checkbox"/> DTIC USERS		21. ABSTRACT SECURITY CLASSIFICATION UNCLASSIFIED	
22a. NAME OF RESPONSIBLE INDIVIDUAL J. D. Huba		22b. TELEPHONE (Include Area Code) (202) 767-3630	22c. OFFICE SYMBOL Code 4780

## CONTENTS

I.	INTRODUCTION .....	1
II.	DISCUSSION OF THE SIMULATION .....	3
	A. Hydrodynamics .....	3
	B. Geometry .....	7
	C. Thermal Conduction .....	9
	D. Equation of State .....	12
	E. Radiation .....	14
	F. Chemistry .....	16
III.	SAMPLE RUNS .....	19
	A. Standard Model .....	19
	B. Comparisons with other Models .....	23
	C. Further Results .....	26
IV.	SUMMARY .....	27
	ACKNOWLEDGMENTS .....	30
	REFERENCES .....	46

Accession For	
NTIS GRA&I	<input checked="" type="checkbox"/>
DTIC TAB	<input type="checkbox"/>
Unannounced	<input type="checkbox"/>
Justification _____	
By _____	
Distribution/ _____	
Availability Codes	
Dist	Special
A-1	23



# NUMERICAL SIMULATION OF THE LASER-TARGET INTERACTION AND BLAST WAVE FORMATION IN THE DNA/NRL LASER EXPERIMENT

## I. INTRODUCTION

Over the past several years the Plasma Physics Division at the Naval Research Laboratory has developed an experimental apparatus which is intended to simulate certain physical processes characteristic of a high altitude nuclear explosion (HANE)<sup>1</sup>. This program is under the auspices of the Division of Atmospheric Effects of the Defense Nuclear Agency. It has the primary goal of a physical understanding and reliable prediction of the degradation of radar and communication systems through a HANE-disturbed environment.

The first series of experiments (ending March 1985) were initiated by irradiating one side of a thin foil target with a neodymium laser. Dark-field shadowgraphy for the case of a high pressure ( $> 1$  Torr) ambient gas taken at 50 to 150 nsec after the laser pulse show that the rapid heating and evaporation of the target material is followed by a blast wave expanding toward the laser<sup>2,3</sup>, here denoted as the forward direction. Except for the pronounced aneurism, which is found at high pressures ( $\sim 5$  Torr) and generally occurs near the laser axis, the blast wave appears quite smooth. On the other hand for those targets supported by a stalk, shadowgraphy reveals that the rearward moving blast wave is very disrupted with many small flocculi. The forward aneurism and rearward flocculi are relevant to the question of whether structure can be seeded in the early stages of blast wave

Manuscript approved January 29, 1986.

formation. To understand the mechanisms responsible for these observed features it is clearly necessary to have a realistic model for the initial laser-target interaction and the subsequent formation of the blast wave. This report presents the results of a numerical simulation of these different stages. The code includes a number of pertinent physical processes in order to provide a complete qualitative picture of the dynamics. Existing measured data on the electron number density and spectroscopy can be used for quantitative verification of the numerical simulation. Since the code is one dimensional it cannot directly answer the question of early time structure, but it is a step toward a global model for the DNA/NRL laser experiment and, as such, can be used as a framework for more detailed studies.

The results from the numerical models show a hot ( $T_e$  -30-70 eV), dense ( $n_e$  -few  $\times 10^{17}$   $\text{cm}^{-3}$ ) cavity pushing on the forward moving blast wave after -50 nsec. At this time the engulfed ambient mass is much larger than the amount of ablated material. The gross structure of this forward half of the blowoff is similar to an isothermal, Taylor-Sedov blast wave and the outflow within the cavity is subsonic. This cavity however, is filled with  $\text{Al}^{+9}$ ,  $\text{Al}^{+10}$ ,  $\text{Al}^{+11}$ ,  $\text{N}^{+5}$ , and  $\text{N}^{+6}$ , indicating a highly non-equilibrium plasma. On the rear side, the blast wave is colder and denser and it is found to satisfy a Rayleigh-Taylor instability criterion at - 40 nsec. This is roughly the time when the rearward accelerated debris has swept-up an equivalent target mass. The overall results further suggest that the radiating line cores should be optically thick.

In the next section we discuss the code in detail by enumerating the physical processes included in it. In section III we describe a standard run and make comparisons with other runs which employ ad hoc assumptions for chemistry and radiative line transfer. In the final section we summarize our main conclusions and make comparisons with the experiment. The limitations of the present code are also presented here.

## II. DISCUSSION OF THE SIMULATION

### A. Hydrodynamics.

The basic hydrodynamic equations to be solved are the continuity equation,

$$\frac{\partial \rho}{\partial t} + \nabla \cdot \rho \mathbf{v} = 0, \quad (1)$$

the total momentum equation,

$$\rho \frac{\partial \mathbf{v}}{\partial t} + \rho \mathbf{v} \nabla \cdot \mathbf{v} + \nabla (p_i + p_e) + \nabla : \mathbf{Q}_{vis} = 0, \quad (2)$$

the ion internal energy equation,

$$\frac{\partial}{\partial t} (\rho \epsilon_i) + \nabla \cdot \mathbf{v} \rho \epsilon_i + p_i \nabla \cdot \mathbf{v} + (\mathbf{Q}_{vis} : \nabla) \mathbf{v} + \nabla \cdot \mathbf{q}_i = Q_{ie} \quad (3)$$

and the electron internal energy equation,

$$\frac{\partial}{\partial t} (\rho_e \epsilon_e) + \nabla \cdot \mathbf{v} \rho_e \epsilon_e + p_e \nabla \cdot \mathbf{v} + \nabla \cdot \mathbf{q}_e = -Q_{ie} + \Lambda + H_L. \quad (4)$$

Here  $\rho$  is the total mass density,  $\rho_e$  is the electron mass density,  $\mathbf{v}$  is the mass velocity,  $p_i$  and  $p_e$  are the ion and electron pressure,  $\mathbf{q}_i$  and  $\mathbf{q}_e$  are the ion and electron thermal conduction,  $\epsilon_i$  and  $\epsilon_e$  are the ion and electron specific internal energies,  $\Lambda$  is the electron energy change due to radiation and ionization, and  $H_L$  is the electron heating due to absorption of the laser energy to be described below (eqn.[30]).  $Q_{ie}$  is the thermal equilibration term from Braginskii<sup>4</sup>

$$Q_{ie} = 3 \frac{\rho_e}{m_i \tau_e} k_B (T_e - T_i), \quad (5)$$

where  $m_i$  is the mean ion mass and  $\tau_e$  is the electron collision time.  $Q_{vis}$  is a tensor artificial viscosity added to smooth out shocks and it has the form suggested by Noh<sup>5</sup> including an artificial heat flux near shocks. A tensor product involving the artificial viscosity is denoted by a colon. We have also assumed that there are no currents so that the ion and electron velocities are equal.

We will limit our analysis so that the variables depend on time and only one spatial coordinate in a general orthogonal coordinate system. Let this coordinate be  $\xi_1$  and the scale factors be  $h_1$ ,  $h_2$ , and  $h_3$ . Then with  $v = ve_1$ ,  $q = qe_1$ , and  $Q = Qe_1e_1$  one finds for the continuity, momentum, and internal energy equations,

$$\frac{\partial \rho}{\partial t} + \frac{1}{h_1 h_2 h_3} \frac{\partial}{\partial \xi_1} (h_1 h_2 h_3 \rho v) = 0, \quad (6)$$

$$\frac{\partial \rho v}{\partial t} + \frac{1}{h_1 h_2 h_3} \frac{\partial}{\partial \xi_1} (h_2 h_3 \rho v^2 + Q_{vis}) + \frac{1}{h_1} \frac{\partial}{\partial \xi_1} (p_i + p_e) = 0, \quad (7)$$

$$\begin{aligned} \frac{\partial}{\partial t} (\rho \epsilon_i) + \frac{1}{h_1 h_2 h_3} \frac{\partial}{\partial \xi_1} [h_2 h_3 (\rho \epsilon_i v + q_i)] + \frac{p_i}{h_1 h_2 h_3} \frac{\partial}{\partial \xi_1} (h_2 h_3 v) \\ + Q_{vis} \frac{1}{h_1} \frac{\partial v}{\partial \xi_1} = Q_{ie}, \end{aligned} \quad (8)$$

and,

$$\begin{aligned} \frac{\partial}{\partial t} (\rho \epsilon_e) + \frac{1}{h_1 h_2 h_3} \frac{\partial}{\partial \xi_1} [h_2 h_3 (\rho \epsilon_e v + q_e)] + \frac{p_e}{h_1 h_2 h_3} \frac{\partial}{\partial \xi_1} (h_2 h_3 v) \\ = -Q_{ie} + \lambda + H_L. \end{aligned} \quad (9)$$

Let us define the area as

$$A(\xi_1) = \iint h_2 h_3 d\xi_2 d\xi_3 \quad (10)$$

where the integration limits extend over the allowed range in  $\xi_2$  and  $\xi_3$ . Now note that for an arbitrary function  $X(\xi_1)$ ,

$$\begin{aligned} \iiint \frac{\partial X}{\partial t} dVol &= \iiint \frac{\partial X}{\partial t} h_1 h_2 h_3 d\xi_1 d\xi_2 d\xi_3 = \int \frac{\partial X}{\partial t} Ah_1 d\xi_1, \\ &= \frac{D}{Dt} \int X Ah_1 d\xi_1 - (AXv) \Big|_{\xi_1=a}^{\xi_1=b}, \end{aligned}$$

where the range of integration over  $\xi_1$  is a to b and  $D/Dt$  is the time derivative following the fluid. Integrating each equation (6)-(10) over a volume element and using the above relation gives

$$\frac{D}{Dt} \int_a^b \rho Ah_1 d\xi_1 = 0, \quad (11)$$

$$\frac{D}{Dt} \int_a^b (\rho v Ah_1) d\xi_1 + \int_a^b A \frac{\partial(p_i + p_e)}{\partial \xi_1} d\xi_1 + (AQ_{vis}) \Big|_a^b = 0, \quad (12)$$

$$\begin{aligned} \frac{D}{Dt} \int_a^b (\rho \epsilon_i Ah_1) d\xi_1 + \int_a^b p_i \frac{\partial(Av)}{\partial \xi_1} d\xi_1 + (Aq_i) \Big|_a^b \\ + \int_a^b AQ_{vis} \frac{\partial v}{\partial \xi_1} d\xi_1 = \int_a^b q_{ie} Ah_1 d\xi_1, \end{aligned} \quad (13)$$

and,

$$\begin{aligned} \frac{D}{Dt} \int_a^b (\rho_e \epsilon_e Ah_1) d\xi_1 + \int_a^b p_e \frac{\partial(Av)}{\partial \xi_1} d\xi_1 + (Aq_e) \Big|_a^b \\ = \int_a^b (-q_{ie} - \Lambda + H_L) Ah_1 d\xi_1. \end{aligned} \quad (14)$$

Equations (11)-(14) are differenced on a Lagrangian grid where  $\rho$ ,  $\rho_e$ ,  $\epsilon_i$ ,  $\epsilon_e$ ,  $p_i$ , and  $p_e$  are carried at the cell centers and  $v$  is carried at the cell interfaces. There are as many of the above equations as there are cells in the whole grid and the limits of integration for the continuity and internal energy equations are the cell interfaces, while the limits are the cell centers for the momentum equation. The differencing is second order in space and a two step predictor-corrector scheme is used for the temporal advance.

Identifying the kinetic energy of cell  $J+1/2$  with interfaces at  $\xi_J$  and  $\xi_{J+1}$  as

$$\frac{1}{4} M_{J+1/2} (v_{J+1}^2 + v_J^2),$$

one can show through a lengthy algebraic computation that the differencing scheme conserves total energy even though the internal energy is transported. This is valid as long as the velocities at the boundary interfaces are zero.

Due to the large change in volume during the experiment from the target dimensions (a few microns) to the blast wave formation (~1 cm), it is necessary to rezone the grid. This is done each time step by first determining the cells which provide the most stringent Courant condition. An isolated subset of these cells is chosen and the interface between each selected cell and its neighbor is moved in such a way as to relax the Courant condition. The amount by which the interface is moved is determined by conserving total mass, linear momentum and energy.

Finally, we mention that the different terms in the above equations are handled in a time split fashion. The hydrodynamics, including the artificial viscosity are done first, then the thermal conduction and equilibration terms are solved implicitly each time step. With these terms completed the chemical reactions are next computed using an improved ARIS<sup>6</sup> module, and finally the radiation is transported.

## B. Geometry.

The initial configuration of the experiment is a thin, planar disc target which is hit on one side with a laser beam. The blowoff from the ablation then undergoes a divergent expansion into the background gas. Even though the code is one dimensional, i.e., the variables depend on only one coordinate, one would like to properly treat both the initial configuration and the divergent blowoff. Clearly a Cartesian geometry can handle the planar target but not the divergent blowoff. A spherical geometry, as used by Stellingwerf<sup>7</sup> in the code MACH1 to model the laser target interaction, does account for the divergent expansion, but it has other problems. Given that the target material expands in a cone of half-angle  $\theta_0$ , it is impossible for the section of the sphere representing the target to simultaneously have the same area, total mass, density and thickness of the actual target. Moreover, the most limiting factor is the inability of a spherical geometry to account for the acceleration and divergence of the rear side of the target after the laser radiation has been absorbed. In such a geometry the rear side implodes toward the center of the coordinate system. Shadowgraphs clearly show that the rear side blowoff is quite different from that of the front side and it is therefore of interest to model.

A spheroidal oblate coordinate system offers the advantage of both a planar initial target and a spherical, divergent expansion. Such a coordinate system can be generated by drawing ellipses in a plane perpendicular to the target face. These ellipses converge to a bar at the target face and tend toward a circle far from the target. The orthogonal set of coordinate lines have an hourglass shape near the target and become spherical rays at large distances. These generating lines are then rotated about an axis through the center of the disc. The axis represents the path of the laser beam. One of these hourglass-shaped generating lines is chosen.

as the lateral boundary of the expanding material. Figure 1 is a sketch of the geometry and initial configuration. The coordinate transformation to cartesian coordinates is given by

$$\begin{aligned}x &= (s^2 + a^2)^{1/2} \cos\psi \cos\phi , \\y &= (s^2 + a^2)^{1/2} \cos\psi \sin\phi ,\end{aligned}$$

and

$$z = s \sin\psi, \tag{15}$$

where  $0 \leq s < \infty$ ,  $-\pi/2 \leq \psi \leq \pi/2$ , and  $0 \leq \phi \leq 2\pi$ . In terms of the discussion of oblate spheroidal coordinates given by Arfken<sup>8</sup>,  $s = a \sinh(u)$ . The flow variables are taken to depend on the distance  $s$  and a fixed  $\psi_0$  determines the hourglass-shaped lateral boundary. From early observations of the experiment, the major portion of the target material expands into a cone of half-angle  $40^\circ$ . Thus  $\psi_0 = 40^\circ$ , and the radius of the target disc ( $r_t$ ) that is irradiated by the laser is related to the parameter  $a$  by

$$r_t = a(1 - \sin^2\psi_0)^{1/2}. \tag{16}$$

The corresponding scale factors are

$$h_s = (s^2 - a^2 \sin^2\psi)^{1/2} / (s^2 + a^2)^{1/2},$$

$$h_\psi = (s^2 + a^2 \sin^2\psi)^{1/2},$$

and

$$h_\phi = (s^2 + a^2)^{1/2} \cos\psi. \tag{17}$$

From these the elemental area and volume are given by

$$\begin{aligned}
 A(s) &= \int_{\psi_0}^{\pi/2} d\psi \int_0^{2\pi} d\phi h_\psi h_\phi, \\
 &= \pi a (s^2 + a^2)^{1/2} \left[ (1 + s^2/a^2)^{1/2} - \sin\psi_0 (\sin^2\psi_0 + s^2/a^2)^{1/2} \right. \\
 &\quad \left. - \frac{s^2}{a^2} \ln \left[ \frac{\sin\psi_0 + (\sin^2\psi_0 + s^2/a^2)^{1/2}}{1 + (1 + s^2/a^2)^{1/2}} \right] \right], \quad (18)
 \end{aligned}$$

and

$$\begin{aligned}
 \text{Vol} &= \int_{s_1}^{s_2} ds \int_{\psi_0}^{\pi/2} d\psi \int_0^{2\pi} d\phi h_s h_\psi h_\phi, \\
 &= \frac{2\pi}{3} \left[ (s_2^3 - s_1^3)(1 - \sin\psi_0) + a^2 (s_2 - s_1)(1 - \sin^2\psi_0) \right]. \quad (19)
 \end{aligned}$$

### C. Thermal Conduction.

The electron thermal conduction has long been known to present a problem in laser-target interactions<sup>9</sup>. The difficulty lies in the fact that the temperature gradient length scale  $L_T = |d \ln(T_e)/dx|$  is on the order of the mean free path  $\lambda$  near the critical surface, while the classical formula for the thermal conductivity assumes  $\lambda/L_T \ll 1$ . The usual approach in fluid codes to rectify this problem has been to limit the heat flux  $q$  such that

$$q = \min \{ -\kappa_{cl} \nabla T_e, -q_{fs} \text{sign}(\nabla T_e) \}, \quad (20)$$

where  $\kappa_{cl}$  is the classical or Spitzer-Harm conductivity, and  $q_{fs}$  is the free streaming limit for thermal heat flux,  $q_{fs} = \alpha n_e k_B T_e (k_B T_e / m_e)^{1/2}$  with typically  $0.03 < \alpha < 0.1$ . A smooth variation in the heat flux can be achieved by using instead

$$q = - \frac{\kappa}{1 + \kappa |\nabla T_e| / q_{fs}} \nabla T_e, \quad (21)$$

with  $\kappa = \kappa_{cl}$ .

It has also been shown by Manheimer<sup>11</sup> that the heat flux can be reduced by turbulence through ion acoustic waves. For  $T_i \ll T_e$ , these waves are driven unstable by the return current of an anisotropic electron distribution function. The criterion for instability can be written as<sup>12</sup>

$$q > F = \frac{3}{2} n_e k_B T_e \left( \frac{k_B T_e}{m_e} \right)^{1/2} \left[ (1 + 3T_i/T_e)^{1/2} \left( \frac{m_e}{m_i} \right)^{1/2} + \left( \frac{T_e}{T_i} \right)^{1/2} [(1 + 3T_i/T_e)^{1/2} - (T_i/T_e)^{1/2}] \exp\left(-\frac{T_e/T_i + 1.5}{1.25}\right) \right], \quad (22)$$

When this condition is satisfied the heat flux can be written as<sup>11</sup>

$$q = - \frac{\kappa_{cl}}{1 + \kappa_{cl} / \kappa_{an}} \nabla T_e, \quad (23)$$

where  $\kappa_{an}$  is the anomalous thermal conductivity due to the turbulence and is given by

$$\frac{\kappa_{cl}}{\kappa_{an}} = \psi = f(Z) \frac{3\pi^2}{2} \frac{n_e \lambda_{De}}{2n\Lambda} \left( \frac{e\phi}{k_B T_e} \right)^2, \quad (24)$$

with  $f(Z)$  a function of the mean charge state  $Z$ ,  $\lambda_{De}$  is the Debye length, and  $\phi$  the potential fluctuations due to the turbulence. The instability saturates by ion trapping with the maximum fluctuation

$$\frac{e\phi_{\max}}{k_B T_e} = \frac{1}{4} \left( \frac{1}{1.25} - 3 \frac{T_i}{T_e} \right)^2. \quad (25)$$

The procedure we use to determine instability is more efficient than that described in Ref. 11 or Ref. 12. From eqns.(22) and (23) we first determine the sign of  $\alpha = q_{cl}/F - 1$ , where  $q_{cl} = \kappa_{cl} \nabla T_e$  and  $F$  is defined in eqn.(22). If  $\alpha \leq 0$ , then the waves are stable and  $\kappa = \kappa_{cl}$ . On the other hand, if  $\alpha$  is positive then the instability is operative. Next the magnitude of the fluctuations is found by setting  $\psi = \min(q_{cl} - 1, \psi_{\max})$ , where  $\psi_{\max}$  is given by eqn.(24) using eqn.(25). This procedure accounts for the saturation in the growth of the unstable waves and gives the marginal stability condition otherwise.

The effect of saturation of the heat flux in steep temperature gradients must still be included, so once having found the value of  $\kappa_{cl}/\kappa_{an}$  we use  $\kappa = \kappa_{cl}/(1 + \kappa_{cl}/\kappa_{an})$  in eqn.(21). In the running of the code it was found that the heat flux saturated near the critical surface but the ion acoustic instability was stable there due to the fast thermal equilibration times. At and in front of the blast wave where the thermal conduction leads to a leading electron temperature foot, the electron heat flux was limited by ion acoustic turbulence as well as being saturated.

A third effect related to the heat flux is its non-local nature in extreme temperature gradients. This aspect has been discussed by Luciani, et al.<sup>13</sup>, but was not included in the present code. Further work on this problem in the presence of large density changes is needed before their expression for the heat flux can be used in the present simulation.

We finally mention that ion heat flux is included in the code and the effect of saturation is treated in a similar manner to that of the electron heat flux. We did not consider any instability which could limit the ion heat flux by turbulence.

#### D. Equation Of State.

The equation of state is different from that of an ideal gas law only in the target material while it remains a solid prior to vaporization. Although the energy required to completely vaporize the target foil is very small compared to the total laser energy in the experiment, neglect of a realistic equation of state for the solid target leads to absurd compressions in the rear side of the target. We do not use a detailed model or table for the solid equation of state, for this would require spending an excessive amount of computer time on transient phenomena. Rather we employ a simple analytic model which adequately accounts for the dominant physical effect, namely the rapid rise in the sound speed in a compressed solid.

The total pressure can be written as<sup>14</sup>

$$p = p_c + p_n + p_e , \quad (26)$$

where subscript c refers to the zero temperature isotherm or cold, solid component, subscript n to the nucleon component (neutrals or ions), and subscript e to the electron component. Let  $\rho_{00}$  be the density of the solid at zero temperature and  $\eta = \rho/\rho_{00}$ , then the internal energy and pressure are related by

$$\epsilon_c = \frac{1}{\rho_{00}} \int_1^\eta p_c n^{-2} dn . \quad (27)$$

Based on formulas (3.4) and (3.20) in Ref.14 we employ the following expressions for the cold pressure:

$$P_c = \begin{cases} C_{32}(\eta^{5/3} - 1) & , \eta \geq 1 \\ C_4 \eta^{2/3} [ e^{C_5(1-\eta^{-1/3})} - e^{C_6(1-\eta^{-1/3})} ] & , \eta \leq 1, \end{cases} \quad (28)$$

where for aluminum  $C_{32} = 4.4 \times 10^{+11}$  ergs/cm<sup>3</sup>,  $C_5 = 7.22$ ,  $C_6 = 3.14$ , and  $\rho_{00} = 2.71$  g/cm<sup>3</sup>. The value of  $C_4$  was taken to be much smaller than  $6.1 \times 10^{+11}$  ergs/cm<sup>3</sup> of Ref. 14, namely,  $C_4 = 1 \times 10^{-7}$  ergs/cm<sup>3</sup>. As can be seen in the P-V-T diagram for aluminum in Fig. D-8 of Ref. 14, there is a deep but narrow well of negative pressure for  $\eta$  slightly less than 1. This feature represents the intramolecular forces which bind a solid together. A large negative pressure can lead to numerical instabilities unless exceedingly small time steps are used. Since the phase of negative pressures is transitory and the internal energy associated with the well is small we can reduce the depth of the pressure well without seriously altering the physics. Further, as the target rarefies due to heating the thermal pressure terms in eqn.(26) readily dominate. From eqns.(27) and (28) and the coefficients  $C_4$ ,  $C_5$ ,  $C_6$  from Ref. 14, one finds that the zero temperature sublimation energy for the target geometry of Fig. 1 is  $8.3 \times 10^{+4}$  ergs, which is much less than the 23 Joules deposited by the laser.

The steep rise of the pressure for compressions does play a significant role in the propagation of shocks through the solid target. In agreement with the results of Schmalz and Meyer-ter-Vehn<sup>15</sup> who used a detailed equation of state, we also found a series of shocks in the target during the early stages of disassembly. These shocks display a small density jump but large pressure changes.

The other terms in eqn.(26) are treated according to the ideal gas law, except initially when the temperature is  $< 0.1$  ev. The P-V-T diagram indicates a constant, low pressure for low temperatures and  $n < 1$ . In these regions the pressure in the solid is taken to be that of the initial ambient gas. This is reasonable since the foil and background gas are in equilibrium before the laser is turned on, while the temperature rapidly increases afterwards.

### E. Radiation.

We begin with a discussion of the initial radiation in the problem, that of the incident laser. The total energy in the laser pulse was set at 23 Joules and a Gaussian shape of 4 nsec full-width half-maximum was adopted. The laser wavelength was  $1.06 \mu\text{m}$ , modeling the output from a neodymium glass laser. The peak intensity of the pulse was  $1 \times 10^{13} \text{ W/cm}^2$  and occurred 5 nsec after the start of the calculation. The pulse was cut off at 10 nsec. The beam energy was deposited using the 1-D radiative transfer equation with inverse bremsstrahlung absorption:

$$\kappa_{\text{IB}} = \frac{(\omega_{pe}/\omega_L)^2}{\sigma_T n_e [1 - (\omega_{pe}/\omega_L)^2]^{1/2}} \quad (29)$$

where  $\omega_{pe}$  is the electron plasma frequency,  $\tau_e$  is the electron-ion collision time, and  $\omega_L$  is the laser frequency. Since the radius of the beam was that of the target disc ( $r_d$ ), the heating rate per unit volume for the electrons in cell J is

$$H_L = \pi r_d^2 I_{J+1} (1 - e^{-\kappa_{IB}^{(J)} \Delta_J}) \frac{1}{\text{Vol}(J)}, \quad (30)$$

where  $I_{J+1}$  is the mean intensity entering cell J of thickness  $\Delta_J$ . The fractional ionization at the front edge of the target is artificially increased at the initial instant of the simulation to provide free electrons. This ensures the absorption of the laser beam since inverse bremsstrahlung depends on the presence free electrons. For simplicity, we neglect reflection of the laser radiation and deposit any remaining incident radiation not absorbed before the critical surface into that cell containing the critical surface. The critical surface is defined as the position where the denominator of eqn.(29) vanishes.

The radiation from the heated gas is treated in several ways. First, bremsstrahlung and recombination radiation are calculated for both the target aluminum material and the ambient nitrogen gas. The recombination radiation is assumed to have a Planck-like spectrum with an effective temperature  $T_{\text{rad}}$ . For cell J this quantity is determined by equating the energy density of a blackbody at  $T_{\text{rad}}$  with the energy emitted by recombination radiation in cell J. Radiation emitted by the nitrogen gas is treated as optically thin, i.e., an energy loss. However, radiation from the aluminum is transported through the entire grid. The radiation transport is calculated by the standard ray-tracing technique in the forward and rearward direction. As shown in the detailed paper by Duston et al.<sup>16</sup>, radiation is a major source of heating for the rear side of the target foil. Hence, since one of our objectives is to simulate the rearward blowoff, it is imperative to correctly calculate the basic energy transport through the entire target. The radiated energy is divided into twelve frequency bins which are chosen to resolve the inner-shell absorption edges of aluminum. The absorption cross sections are from Fig. 2 of Ref. 16. Any radiation that passes through the aluminum gas is

also transported through the ambient nitrogen gas. This results in the dissociation of background  $N_2$ . The absorption cross sections for this process are based on those used in Hyman et al.<sup>17</sup>

Second, excitation line radiation is modelled in two extreme conditions: completely optically thick and optically thin. The optically thick case simply means that any emitted line from a cell J is absorbed in that same cell. No calculation is needed here. For the optically thin case we calculate the emission from 13 resonance lines of aluminum and 14 resonance lines of nitrogen. All ionization stages of both species are covered. Our interest in the line radiation stems from the possibility of cooling in the cavity behind the blast wave. We did not consider the K-lines which originate during the early phase of target vaporization. In calculating the emission from our chosen set of lines, the excited state populations are determined by balancing the collisional excitation rate against the de-excitation rate from the excited state, the ionization rate to the next higher ionization stage, and the radiative decay rate. Optical pumping as well as photoionization of the resonant state due to recombination radiation are not evaluated. These features ensure that the line radiation is not overestimated in the absence of reabsorption.

### F. Chemistry.

Much effort was spent in developing a chemistry module which can handle the extreme range of chemical conditions in the experiment. For simplicity, we do not follow any excited state populations but assume all ions (and neutrals) are in the ground state. Essentially we divided the chemical evolution of the aluminum material into three schemes. First, during a brief initial stage the aluminum undergoes a phase transition from a solid to a

high density gas at  $\leq 1$  ev. Here we use an analytic procedure to determine the temperature and fractional ionization from the internal energy. The analytic solution is based on fits to numerical calculations of an equilibrium aluminum gas with only neutral and singly ionized species. As the target continues to absorb the laser energy, the fractional ionization and temperature drastically increase. Once the fractional ionization increases above 0.8, an iteration on the temperature and ionization level for a given internal energy is employed, again for equilibrium conditions. In this second scheme for the chemical evolution all the ground state ionization levels are included. Finally, when the electron density in any cell falls below  $5 \times 10^{19} \text{ cm}^{-3}$ , the chemistry in that cell is integrated in time using reaction rates, i.e., we allow the population of the ground state levels to fall out of equilibrium. For this third scheme, the ARIS<sup>6</sup> module is used to solve the corresponding set of stiff differential equations. For the nitrogen gas, the chemical evolution is always followed using reaction rates.

The numerical details of this evolution from low temperature, dense equilibrium chemistry to high temperature, rarefied reaction rate chemistry is too complicated to be reported here. We do mention that the transition from one chemistry scheme to the next must be done smoothly. This requires the inclusion of many reaction processes to ensure that the limiting conditions lead to equilibrium results. For instance, at high density and low temperature we reproduce the simple Saha equilibrium by using detailed balance between collisional ionization and 3-body recombination. Such equilibrium is valid only for a high density gas where the dominant recombination process is 3-body. In addition to 3-body recombinations and electron collisional ionization, we also include radiative recombination and dielectronic recombination processes so that the lower density, higher temperature regimes are modeled correctly. A high density correction for

dielectronic recombination rates similar to that used by Jordan<sup>24</sup> is employed.

As an aside on computational physics, the use of a sequence of numerical schemes for the chemistry is most efficiently and correctly employed in a Lagrangian hydrodynamic code. In this approach the decision to switch from one scheme to the next, vis., analytic -> equilibrium -> time dependent, can be made in each individual cell independent of all the others since each cell carries the same material with it. Unfortunately, in a purely Lagrangian code the effects of charge exchange cannot be investigated, for the aluminum debris cannot overrun the nitrogen background. We must thereby limit the simulation results to the high pressure regime where strong coupling between the expanding debris and background occurs.

### III. SAMPLE RUNS

In this section we will present detailed graphical results from the numerical simulations. Four distinct models were studied. The differences in the models lies in the treatment of the chemistry and line radiation. In model A, which we refer to as the standard model, time dependent chemistry is employed and all line radiation is assumed to be optically thick, i.e., no transport of line radiation is considered. In model B, equilibrium chemistry is used and again the line radiation is optically thick. For models C and D the line radiation is taken to be optically thin, but model C has time dependent chemistry and model D has equilibrium chemistry. Recall from section II.F. that equilibrium chemistry is not necessarily LTE but includes the effects of radiative and dielectronic recombination. The objective of studying these four models is: (i), to demonstrate the importance of non-equilibrium chemistry, and (ii), to investigate whether line radiation can realistically cool the cavity inside the blast wave. Since we do not perform a detailed calculation for the transfer of line radiation, the two extremes of optically thick and thin enable one to obtain only qualitative conclusions.

#### A. Standard Model.

Figure 2 shows the position of the blast wave for both the front side and the back side as a function of time for model A, the standard model. The time in this figure is measured from the instant of peak intensity of the laser pulse, which is what the experimentalists use as their zero time. In the code the laser pulse is initiated 5 nsec before the peak. The solid line in Fig. 2 is given by

$$R(\text{cm}) = 0.123 \left[ \frac{E(\text{Joules})}{p(\text{Torr})} \right]^{0.2} [t(\text{nsec})]^{0.4} \quad (31)$$

for  $E = 23$  Joules and  $p = 2.5$  Torr. This equation is from Ref. 3 and describes the observed temporal evolution of the front side of the blast wave. As noted in that reference, the equation for  $R(t)$  has the same temporal and parameter dependence as that for a Taylor-Sedov blast wave. We note the excellent agreement in Fig. 2 between the numerical simulation and the experimental data for the position of the front side blast wave. The blast wave on the back side displays a turbulent structure in the shadowgraphs and no general formula for its position in time has been developed. This turbulent structure will be discussed below in light of the results of the simulation. The equal mass radii ( $R_{EM}$ ) for both the front and back side are also noted in Fig. 2. Specifically,  $0.15 \times 10^{-6}$  g is ablated toward the front side while the remaining  $0.55 \times 10^{-6}$  g is accelerated rearward. As demonstrated by the simulation, the Taylor-Sedov blast wave solution becomes applicable for the front side shock location only after several equal mass radii have been encountered.

In Fig. 3 the energy budget for model A is presented.  $\int E_L dt$  is the accumulated energy deposited by the laser over time. It attains 23 Joules at 10 nsec after the peak of the laser pulse.  $E_K$  is the instantaneous kinetic energy of directed motion while  $E_T$  is the instantaneous thermal (random) energy of all particles. The chemical energy, i.e., the energy locked up in the ionization of aluminum and nitrogen at a given time is denoted by  $E_C$ . Finally,  $\int E_R dt$  is the accumulated energy lost from the system during the run due to recombination and bremsstrahlung radiation. The values in Fig. 3 include both sides of the expanding target. The relation

$$E_K(t) + E_T(t) - E_C(t) - \int_{-5}^0 \text{nsec} \dot{E}_R dt = \int_{-5}^0 \text{nsec} \dot{E}_L dt ,$$

expressing conservation of total energy, is satisfied to within 3% throughout the run. This result is also typical for the other runs discussed below. Nearly all of the energy that is missing during a simulation run occurred in the time dependent chemistry routine.

Note in Fig. 3 that initially the kinetic energy is dominant, but after  $\sim +20$  nsec the fraction in thermal energy is largest and stays at roughly 35%. For an adiabatic Taylor-Sedov blast wave with  $\gamma = 1.1$  (see ref. 3) 90% of the total energy is thermal with the rest being kinetic. This is clearly not the case here and points to the first major difference between the simulation of the experiment and the ideal blast wave theory. This difference is due to the significant amount of energy locked up in ionization potential and the smaller radiated energy. These two energy sinks, which are not included in the ideal Taylor-Sedov model, account for roughly 45% of the total energy in the system. The high fraction of kinetic energy at the end of the run, 20% instead of 10%, arises from the fact that the rear side blowoff is dense and relatively cool.

Figures 4a through 4g show snapshot profiles of different quantities during the standard model simulation. The figure captions fully describe the nomenclature and symbols used to present the numerical data. Here we will point out a few salient features.

Note first of all that the time shown on the graphs refers to the simulation time which is zero when the laser turns on. To transform to the time from the peak intensity of the laser pulse subtract 5 nsec. Figure 4a displays the situation at the initial instant of the simulation; the aluminum is at solid density of  $6 \times 10^{23}$  atoms/cm<sup>3</sup> and the ambient nitrogen is at  $3.5 \times 10^{17}$  molecules/cm<sup>3</sup>. Both materials are predominantly neutral, but a thin partially ionized region at the front of the target is imposed to ensure that the laser beam is absorbed by inverse bremsstrahlung. Note that the

abscissa is in Lagrangian cell units in order to expand the target region for clarity.

Figures 4b, 4c, and 4d display the situation shortly after the peak of the laser pulse again in Lagrangian cell units. The critical surface occurs near the peak of the electron density and temperature (see Fig. 4b). One can clearly see, from the plot of the artificial viscous pressure  $Q$ , a series of shocks traversing the aluminum target. This feature agrees with the detailed equation of state study of Ref. 15. The heating of the back side of the target is due to these shocks as well as to the absorption of radiation emitted from a region near the critical surface. The graph of the mean charge state in Fig. 4c,  $n_e/(n_i + n_n)$ , shows that highly ionized aluminum, namely  $Al^{+9}$ ,  $Al^{+10}$ , and  $Al^{+11}$ , is created early on in the laser target interaction. We find that during the subsequent stages of forward blowoff and cavity formation the aluminum does not have enough time to recombine and remains in these highly ionized states. Since the cavity temperature drops below 100 eV, this non-equilibrium ionization structure points out the importance of using a non-LTE, time dependent chemistry in the simulation. The spectrum in Fig. 4d only includes the radiation from recombination and bremsstrahlung; it displays some of the qualitative features of Figure 11 in Ref. 16 but clearly the lack of a detailed treatment of the recombination spectrum and lines represents a limitation of our present model.

Figure 4e is a snapshot of the flow variables at the time when the forward moving blowoff has swept up one equal mass of ambient material. The abscissa is now given in physical space since the target has expanded sufficiently to be resolved. The formation of a reverse shock at this time on this front side can be seen from the peak in the artificial viscosity ( $Q$ ) in the aluminum material. Note that radiation and thermal conduction have raised the electron temperature of the ambient nitrogen on the front side and a thermal foot leading the main shock is present there.

Figures 4f and 4g show the long time development of the system out till the forward moving blast wave reaches the boundary of the calculational grid. From the density plot in Fig. 4f one finds that the blast wave thickness, as measured by the width of the peak in the electron density profile, is roughly twice as thick as the experimentally observed value of 3% of the blast wave radius<sup>3</sup>. However, the peak electron density in the shock of  $4 \times 10^{+18} \text{ cm}^{-3}$  is typical of the reported measurements from several interferograms<sup>18</sup>. Moreover, the mean electron density in the cavity of a few times  $10^{+17} \text{ cm}^{-3}$  is in good agreement with the recent, though tentative, measured value of  $2 \times 10^{+17} \text{ cm}^{-3}$  at 60 nsec after the peak of the laser pulse<sup>19</sup>. The surprisingly high value for the electron density reflects the high degree of ionization of the aluminum debris in the cavity; note that the ion density in the cavity is much smaller. From the viscous pressure plot in Fig. 4f the reverse shock on the front side has moved back toward the original target position and the formation of a second reverse shock in the backward moving aluminum is also evident. By the time of Fig. 4g the cavity between the forward and backward moving blast waves is nearly isothermal with  $T_e = 60 \text{ ev}$ . This is the second major difference of the simulation results from the ideal, adiabatic Taylor-Sedov blast wave wherein the temperature rises as one moves inward from the blast wave. Actually the run of the velocity and ion density on the front side looks quite like the solution for an isothermal Taylor-Sedov blast wave as discussed in Ref. 20. The isothermality is mainly due to electron thermal conduction. We note for reference that an isothermal blast wave also evolves according to a  $t^{0.4}$  law.

### B. Comparisons With Other Models.

Figures 5a, 5b, and 5c show snapshots of the flow variables for models B, C, and D, respectively. Each of these graphs is at a time close to 50

nsec in simulation time and can be compared with Fig. 4f. The distinction between these models and the standard one (model A) is noted in Table I which contains some of the gross characteristics for each model. The figures and table will be discussed together. The main differences between the time-dependent (model A) and equilibrium chemistry (model B) are the lower electron temperature in the cavity (65 ev for model A vs. 90 ev for model B) and the higher mean ionization level in the cavity (9.7 for model A vs. 7.5 for model B). These differences arise because the equilibrium model allows sharing between ionization and thermal energy with no regard for time scales. When we assume that the radiation from the resonance lines is optically thin, as in models C and D, we find a significant increase in the percentage of radiation lost from the system. The values of 61% and 38% are much higher than the experimentally estimated 25% radiation energy loss when the MRC gas mixture was used for the ambient material. Since the MRC mixture is a much more efficient radiator than a pure nitrogen gas we surmise that the resonance lines cannot be optically thin. Simple estimates for the optical depth of a Doppler broadened line also show that the optical depth is greater than one for the cavity conditions. Furthermore, Figs. 5b and 5c indicate too thin a blast wave and too high a peak electron density, when compared against the observations. This is especially true for model C.

TABLE I

## COMPARISON OF DIFFERENT MODELS

 $(E_L = 23 \text{ Joules}, p_0 = 2.5 \text{ Torr}, t = 50 \text{ nsec})$ 

		A	B	C	D
		Time dep. chem. No line rad.	Equil. chem. No line rad.	Time dep. chem. Line rad.	Equil. chem. Line rad.
Energy	$E_K$	23%	24%	16%	23%
Budget:	$E_T$	37%	35%	11%	23%
	$E_C$	21%	21%	12%	15%
	$E_R$	19%	20%	61%	38%
Shock:	$R(\text{cm})$	0.90	0.89	0.88	0.86
	$n_e(\text{cm}^{-3})$	$4 \times 10^{+18}$	$6 \times 10^{+18}$	$18 \times 10^{+18}$	$10 \times 10^{+18}$
Cavity:	$T(\text{ev})$	65	90	30	70
	$n_e(\text{cm}^{-3})$	$2 \times 10^{+17}$	$2 \times 10^{+17}$	$1.5 \times 10^{+17}$	$2 \times 10^{+17}$
	$n_e/n_{Al}$	9.7	7.5	9.7	7.0
	$n_e/n_N$	4.5-5	4.5-5	3-4.5	3-4.5

### C. Further Results.

The experimentally observed flocculi on the backside blowoff is very distinct from the smooth front side. Within the confines of a one dimensional calculation it is impossible to model such turbulence; however, we find that the conditions for a Rayleigh-Taylor instability are satisfied in the back side blast wave. It is possible that such an instability leads to the observed structure and we present the numerical results of a linear analysis below.

Specifically, the Rayleigh-Taylor instability arises from the deceleration of the aluminum debris by the less dense ambient nitrogen. This deceleration occurs when the rearward moving debris has swept up about an equal mass of the ambient material. The growth rate for the decelerating Rayleigh-Taylor instability is given by

$$\omega = \left[ \frac{DV}{DT} \cdot \nabla \ln(\rho) \right]^{1/2}, \quad (32)$$

where  $\omega$  is the growth rate. This expression is calculated at each interface between cells and the expression for the temporal velocity derivative includes the pressure gradients and the artificial viscosity terms in eqn.(12). Whenever  $\omega$  is real the interface is unstable. The resultant growth rates ( $\omega$  real) for four different times in the standard model are presented in Figure 6. At an early phase in the simulation the front side contact discontinuity, located at the right vertical line near cell #41, is seen to be unstable. However the duration of the conditions for a positive growth rate last only a couple of e-folding times, and by 55 nsec the front contact discontinuity is essentially stable. (Isolated crosses are not considered to be indicative of consistent conditions for Rayleigh-Taylor growth but rather transient phenomena.) On the other hand, from roughly 20 nsec to at least 55 nsec the rearside contact discontinuity, at the left

vertical line near cell #20, is Rayleigh-Taylor unstable. This temporal duration is sufficient for several e-folding times. As can be seen from Fig. 2, this time span centers around the time of one equal mass radius for the back side blowoff. We suggest that the flocculi observed in the shadowgraphs at - 50 nsec and beyond are due to this Rayleigh-Taylor deceleration instability. The continuation of the turbulence into late times emerges from the sufficient number of e-folding times for this instability on the rear side. At very early times, say 10 to 20 nsec, the front side may also exhibit some structure, but the limited number of e-folding times for this region would not lead to non-linear effects.

For completeness, we display the local Mach number at four different times for the standard model in Figure 7. The results are related to the proposed use of small obstacles as a probe of the cavity dynamics<sup>21</sup>. Beyond about 20 nsec the major portion of the cavity between the forward and backward moving blast waves is subsonic. This result predicts that a bow shock formed about a small obstacle at the time it is overrun by the forward moving blast wave will dissipate into a sound wave as the expansion continues.

#### IV. SUMMARY

We have presented the details of a one dimensional numerical simulation code intended to model the NRL laser/HANE experiment in the high pressure regime ( $p_0 > 1$  Torr). Although the code is one dimensional and cannot model the development of instabilities and the self-generated magnetic fields, a large number of physical processes have been modeled in order to study the gross physical characteristics of the experiment. These features include an oblate spheroidal geometry to account for the rearward expansion, electron and ion thermal conduction with saturation including the limiting effects of

the ion-acoustic instability on electron thermal conduction, an equation of state representative of solid aluminum during the target disassembly, radiation transfer for the continuum and bremsstrahlung radiation originating in the aluminum material, and an intricate chemistry which spans the range from LTE to highly non-equilibrium conditions.

Other numerical codes have studied the laser-target interaction problem in 2-D with accurate radiation transport and/or self-generated magnetic fields, such as that of Colombant, et al.<sup>25</sup>, Brackbill and Goldman<sup>26</sup>, and Pert<sup>27</sup>. These codes are constructed to simulate the first few hundred picoseconds of the interaction, before any hydrodynamic reaction of the background plasma. The emphasis of the present laser/HANE experiment is primarily on the coupling of the debris to the background gas which takes place over a timescale of tens of nanoseconds. The code we have described concentrates on the latter, longer timescale phenomena, and hence is significantly different from the previous codes. For instance, the use of a Lagrangian grid or adaptive rezoning is necessary to follow the great change in length scales from the target size to one centimeter: the above referenced codes employed a fixed Eulerian grid for the hydrodynamics. The extension of the present numerical techniques to a 2-D code is clearly necessary to improve the radiation transport, to study instabilities, and to include the effects of the self-generated magnetic field on thermal conduction. The present model is an initial step toward a more complex 2-D one and the results, listed below, point out specific features which a more advanced code should further study.

The primary results from the present numerical simulation are as follows.

(1) For the standard model (A) the cavity behind the forward moving blast wave is hot ( $T_e \approx 60$  eV) and dense ( $n_e \approx 2 \times 10^{17} \text{ cm}^{-3}$ ). The ion temperature in the cavity is about the same as  $T_e$  but the ion density in the

aluminum part of the cavity is a factor of 10 smaller (see Fig. 4f). Overall, the dynamic structure of the forward blowoff region resembles an isothermal Taylor-Sedov blast wave, albeit with a significant amount of energy tied up in chemical potential and radiation losses (see Fig. 3). This result is quite different from the LTE model presented by R. Stellingwerf<sup>22</sup> wherein the cavity is much colder ( $T_e$  - few eV) and rarefied ( $n_i$  - few  $\times 10^{15}$  cm<sup>-3</sup>). Our predicted electron density for the cavity agrees with a tentative measurement by J. Stamper<sup>19</sup>. The electron densities in the blast wave also agree with the measurements<sup>18</sup>.

(ii) Due to the initial rapid heating and the slow recombination rates, the material in the cavity is highly overionized for the local electron temperature. In particular, by 50 nsec the aluminum is mostly Al<sup>+9</sup>, Al<sup>+10</sup>, and Al<sup>+11</sup>, and the nitrogen is mostly N<sup>+5</sup> (see Table I). The latter has been observed in an integrated spectrum<sup>23</sup> and it should be possible to search for the presence of Al<sup>+10</sup> using the same technique. Such an observation would provide a direct verification of our use of a time-dependent chemistry. Due to the limitation of a Lagrangian code, we did not include charge exchange as one of the chemical reactions. If the blast wave becomes leaky for lower ambient pressures ( $p_0 < 1$  Torr), some of these highly ionized particles could penetrate ahead of the blast wave. To model charge exchange and leaky blast waves a two ion fluid code or a particle code would be needed.

(iii) The results of our models which assume optically thin lines (models C and D) indicate an unrealistically large amount of radiation loss (see Table I). This suggests that the resonance lines from the blast wave and cavity are not optically thin, but an improved radiation model with line transport is required to determine how thick the lines are.

(iv) The deceleration Rayleigh-Taylor instability is found to be satisfied at the rear contact discontinuity at the time when an equal mass is

swept up by the rearward moving blast wave (see Fig. 6). We suggest that this instability may be responsible for the flocculi observed on the rear side. Again, a two dimensional code is required to follow the non-linear development of the unstable regions. On the front side the instability is also active, but only for a brief time near 7 - 20 nsec. This span of time allows only a few e-folding times. It would be of interest to take shadowgraph pictures at these early times to discern if the blast wave is initially unstable but later heals itself to the smooth form seen in shadowgraphs at times  $> 50$  nsec. It should be noted that this instability appears to have little to do with the formation of the prominent aneurisms seen on the front side blast wave.

(v) Due to the high temperature in the forward half of the cavity the flow is subsonic. A bow shock formed about a small, stationary obstacle to the blast wave would be expected to dissipate into a sound wave with a weaker density jump as the obstacle is engulfed by the expanding cavity.

#### ACKNOWLEDGMENTS

We are grateful to Dr. Ellis Hyman for continued encouragement during the course of the code development and for a detailed reading of an initial draft of this paper. Conversations with Drs. Ed McLean, Chuck Manka and John Stamper were fruitful in focusing our efforts on specific issues. Advice from Dr. Robert Clark on radiation transport and from Dr. John Gardner on the equation of state were particularly helpful. We are especially thankful to Dr. Barry Ripin for his support during this project. This research was funded by the Defense Nuclear Agency.

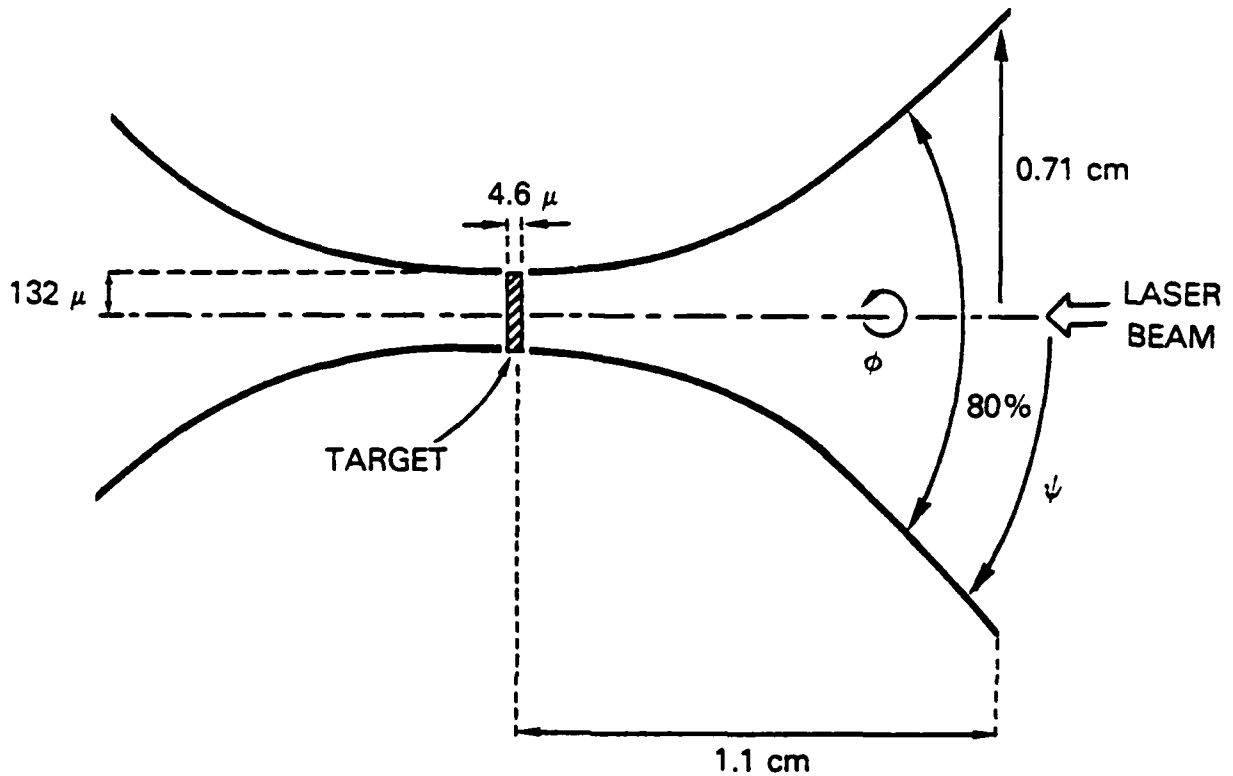


Figure 1. Geometry of target, laser beam, and boundary of oblate spheroidal coordinate system used in the numerical simulation. The system is rotationally symmetric about the laser beam axis. The opening angle for the blowoff asymptotically approaches  $90^\circ$  far from the target. The front and back boundary are each  $1.1 \text{ cm}$  from the target. The target is a disc of radius  $132 \mu$  and thickness  $4.6 \mu$ .

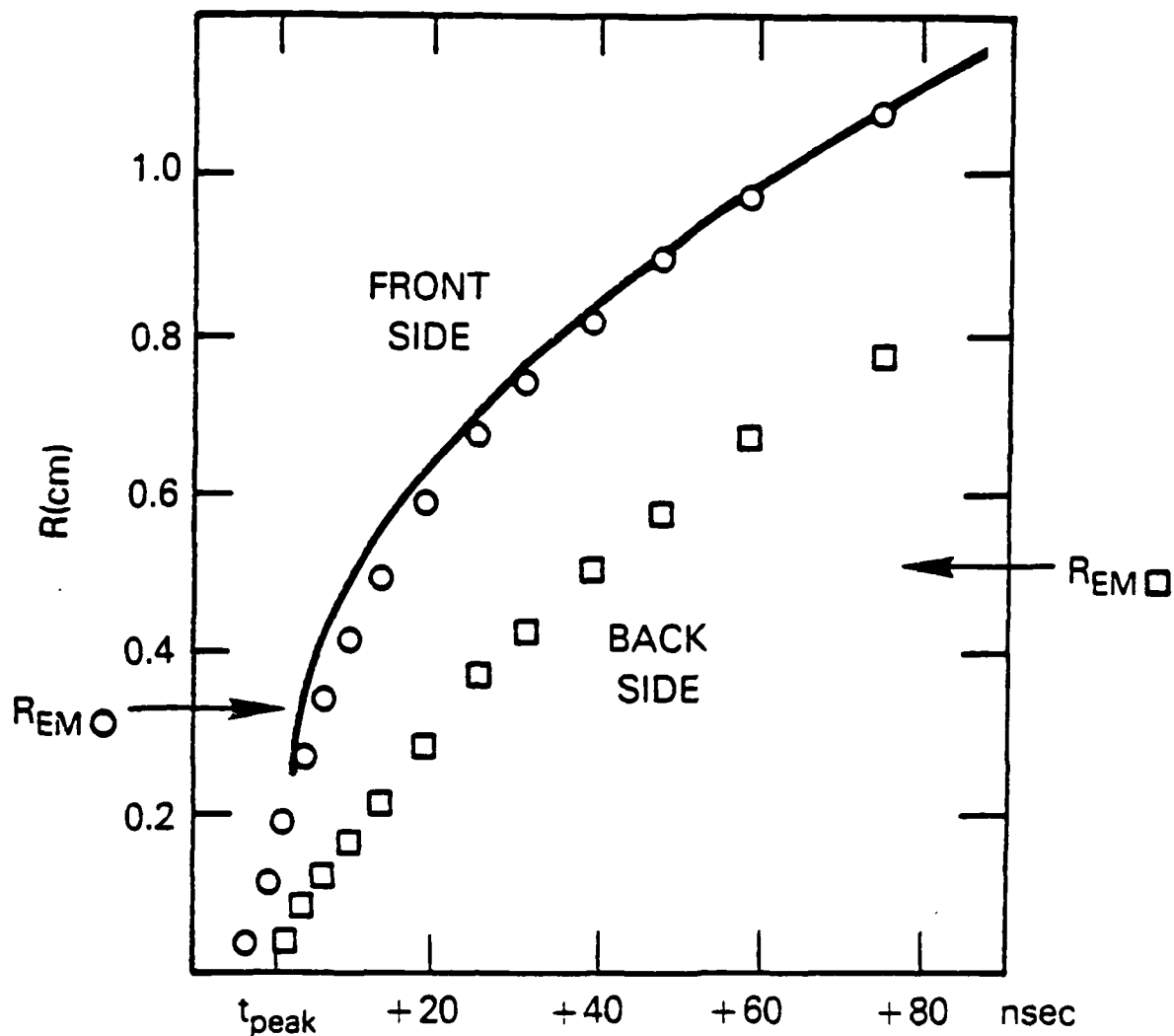


Figure 2. The position of the front side (o) and back side ([]) blast wave for the standard model as a function of time measured from the peak intensity of the laser pulse. The equal mass radii for both sides are also indicated. The solid line is the position of the front side blast wave from the experimental.

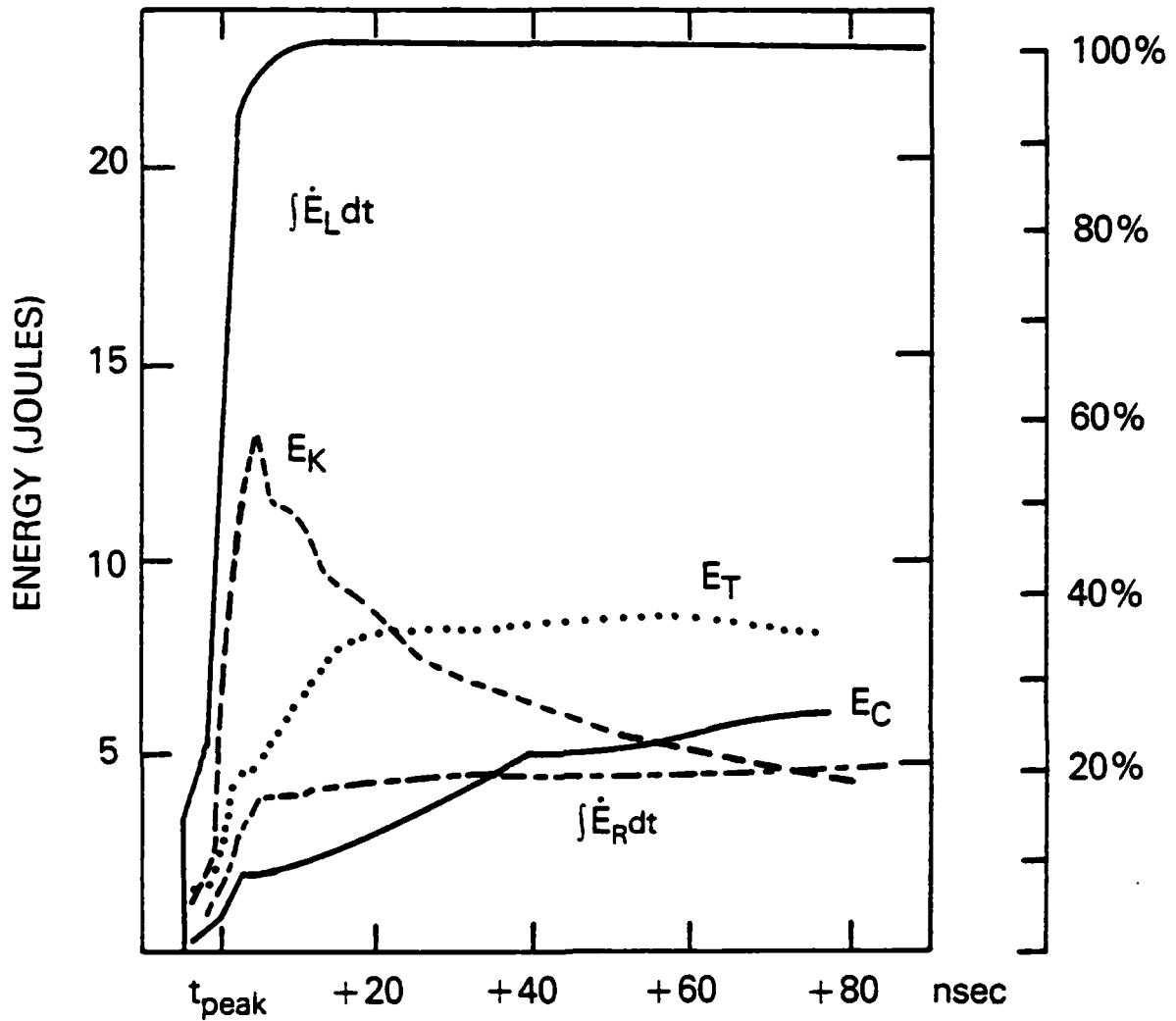


Figure 3. The energy budget for the standard model as a function of time measured from the peak intensity of the laser pulse.  $\int \dot{E}_L dt$  is the accumulated energy input from the laser,  $E_K$  is the instantaneous kinetic energy of directed motion,  $E_T$  is the thermal energy of random motion,  $E_C$  is the chemical potential energy, and  $\int \dot{E}_R dt$  is the accumulated radiated energy.

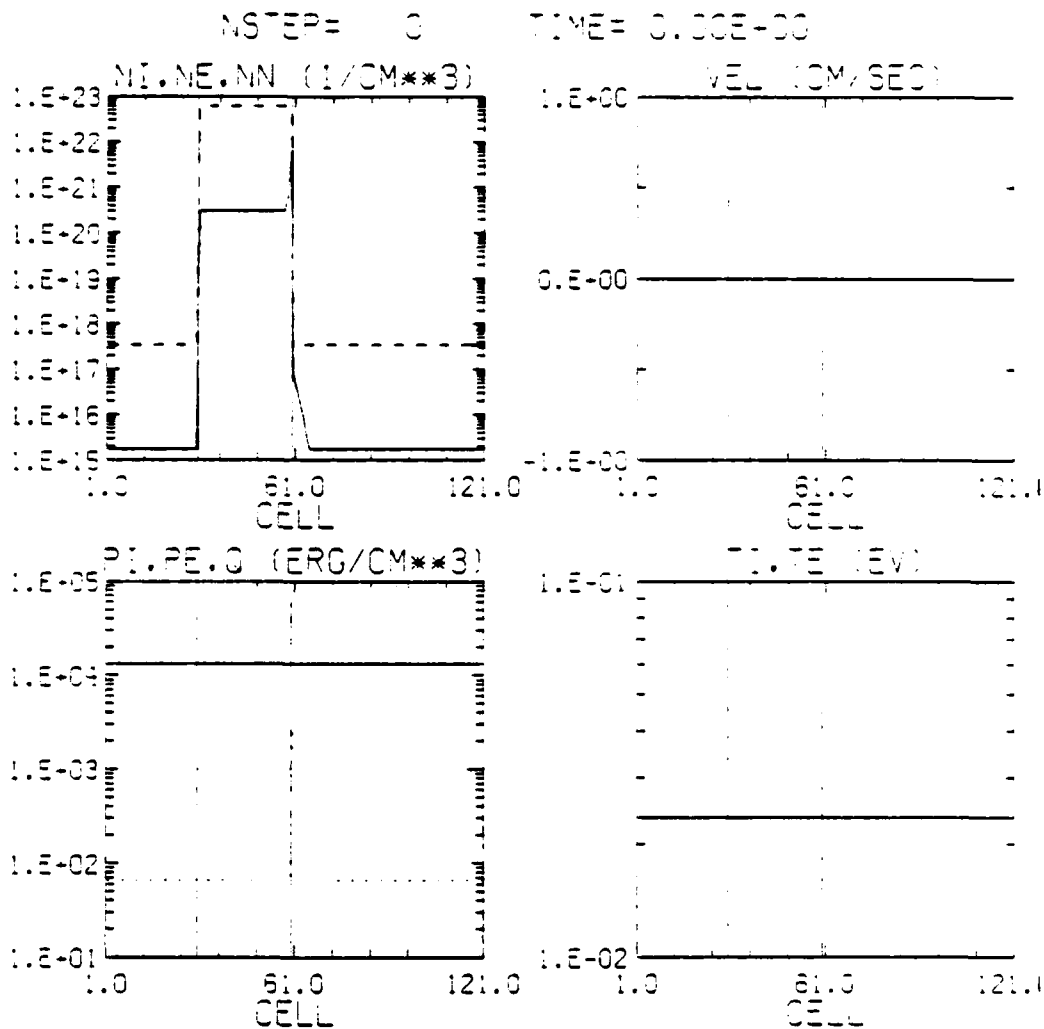


Figure #a. Number density (NI = ions, NE = electrons, NN = neutrals), mass velocity, pressure (PI = ions, PE = electrons, Q = artificial viscosity) and temperature (TI = ions, TE = electrons) for the standard model at the initial time of the simulation. The abscissa is the cell number in the Lagrangian grid.

Throughout these and the following graphs the solid line in each box refers to the first quantity listed at the top of the box; the dotted line to the second quantity, and the dashed line to the third quantity. The straight vertical lines represent the boundaries separating the aluminum and nitrogen material. The aluminum resides between these lines.

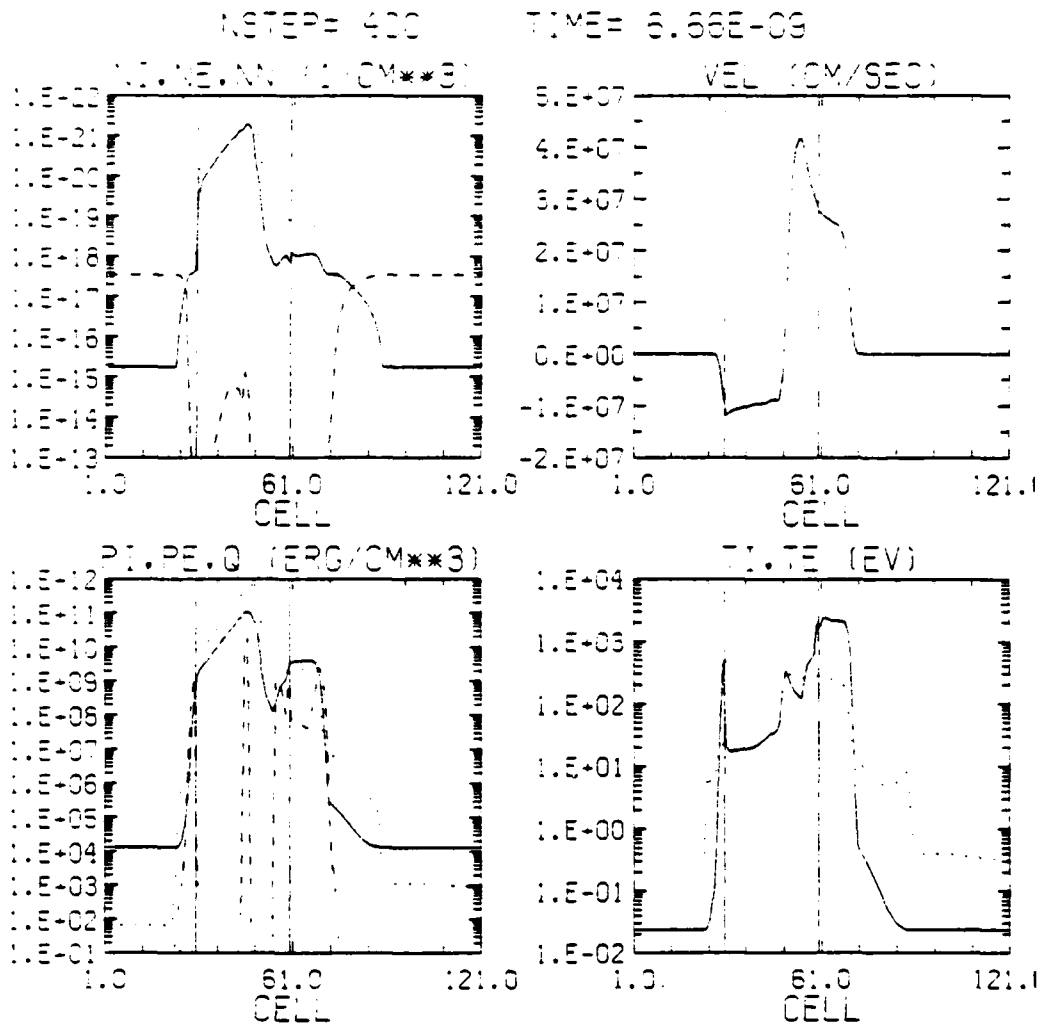


Figure 4b. Same as Fig. 4a except at 6.66 nsec after the start of the simulation.

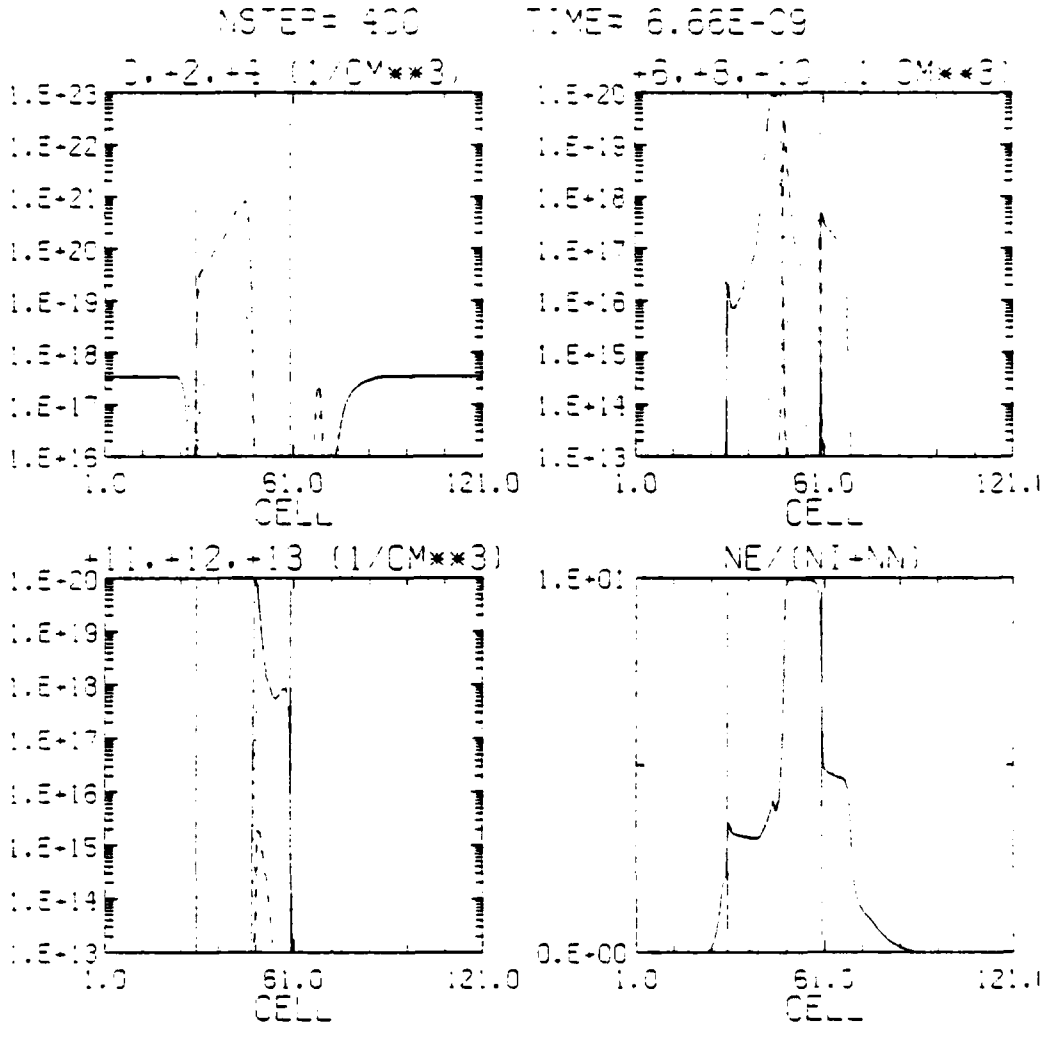


Figure 4c. The number density of different ionic species and the mean charge state at 6.66 nsec.

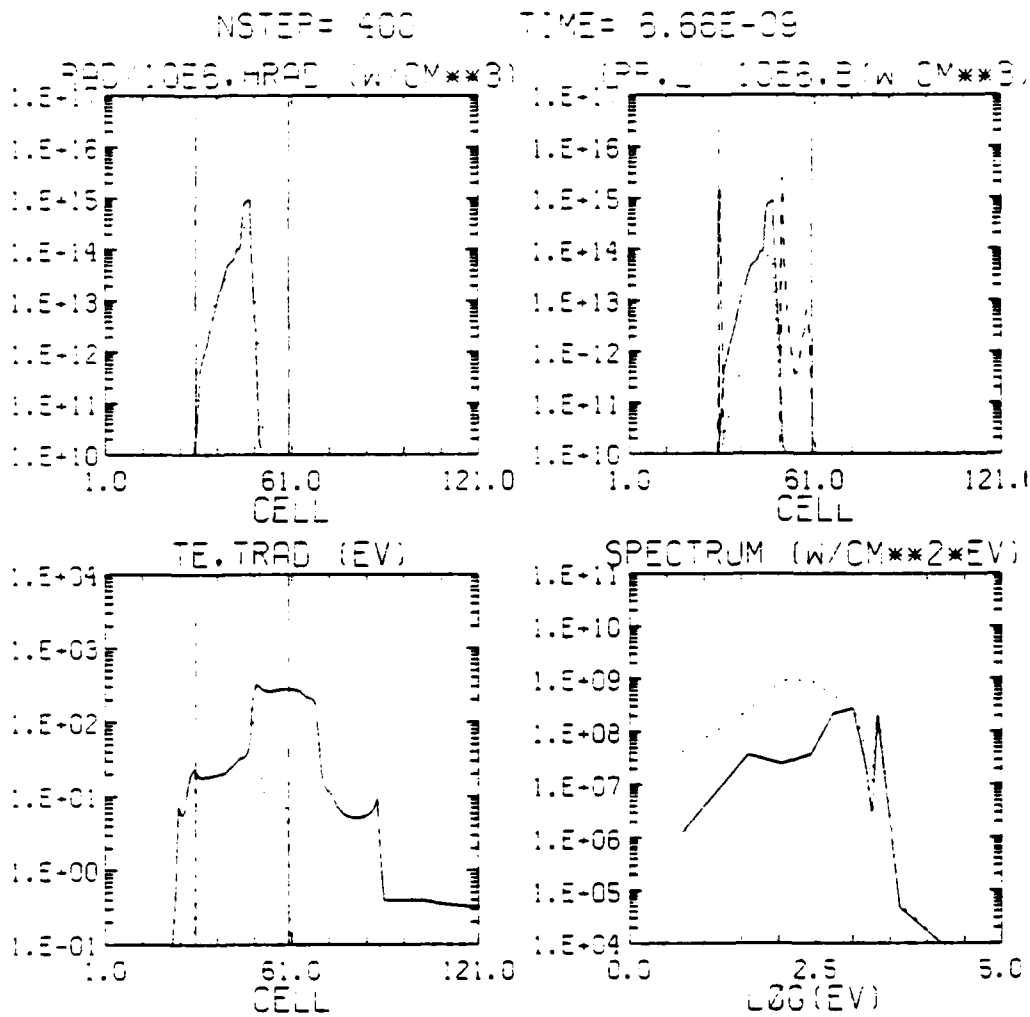


Figure 4d. The top left box shows the rate of emitted radiation per unit volume (RAD divided by  $1 \times 10^6$ ) and the rate of heating per unit volume (HRAD) due to absorption of the radiation. The top right box breaks down the emitted radiation into recombination (RR), line (L), and bremsstrahlung (B). The bottom left box shows the electron temperature (TE) and an effective radiation temperature (TRAD) based on a blackbody flux. The bottom right box shows the smoothed spectrum emerging from the back side (solid line) and front side (dotted line). The simulation time of 6.66 nsec is shortly after the peak intensity of the laser pulse (5 nsec).

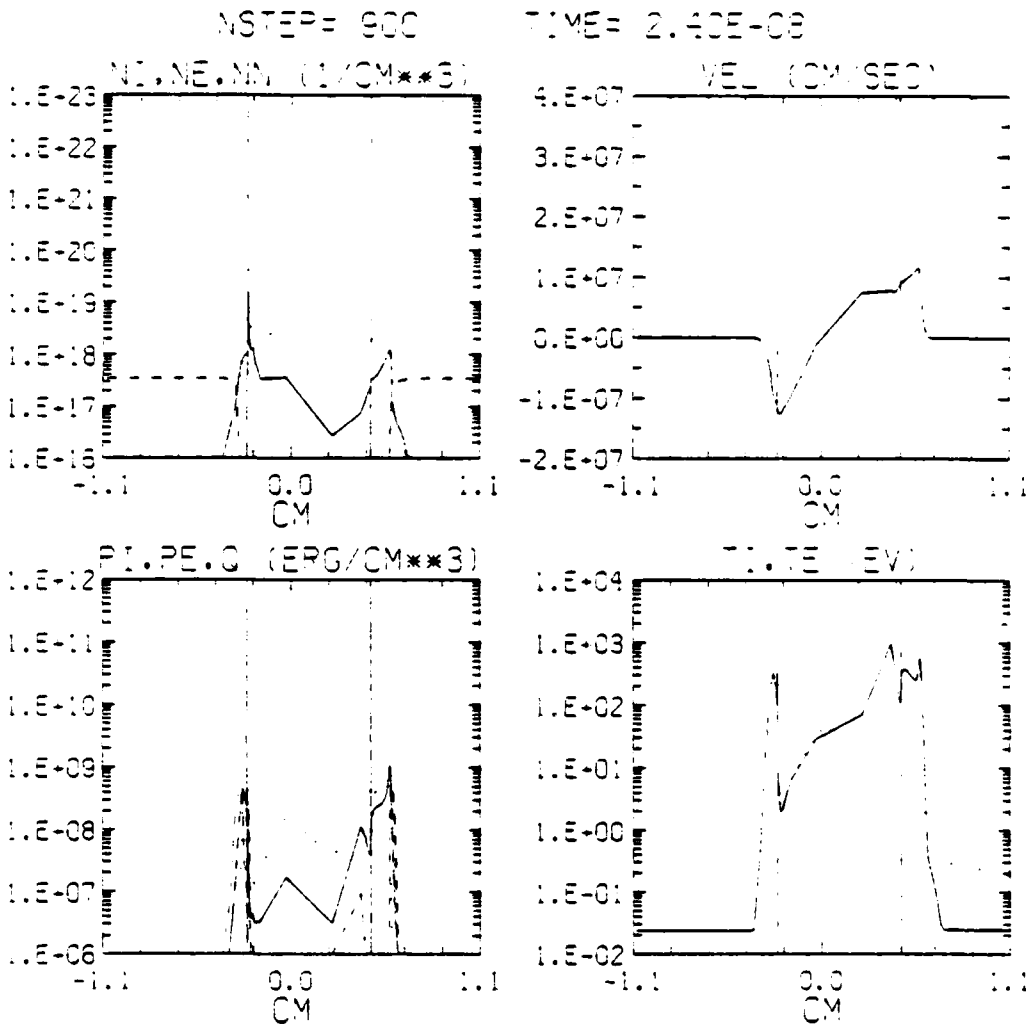


Figure 4e. Number density (NI = ions, NE = electrons, NN = neutrals), mass velocity, pressure (PI = ions, PE = electrons, Q = artificial viscosity) and temperature (TI = ions, TE = electrons) for the standard model at the simulation time 24.0 nsec. The abscissa here and in the following graphs is in physical dimensions.

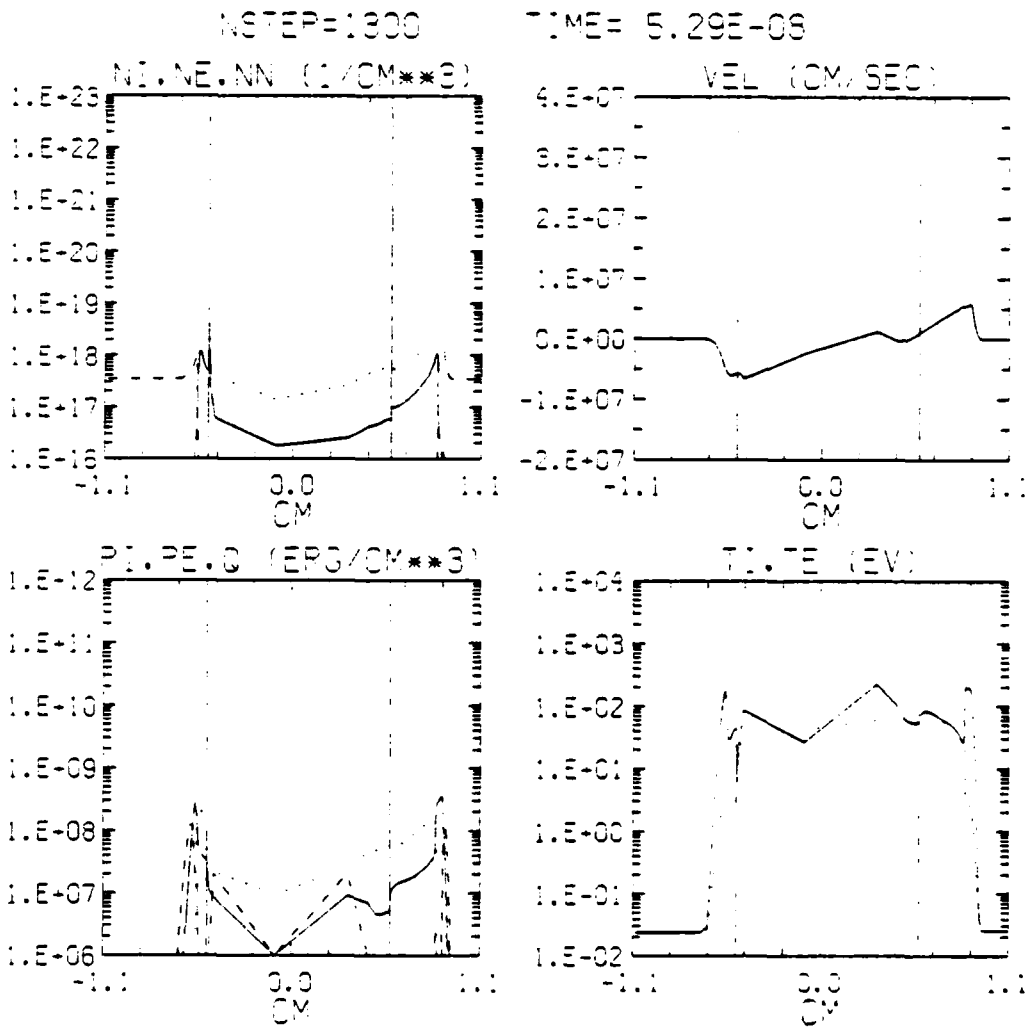


Figure 4f. Same as Fig. 4e except at the simulation time 52.9 nsec.

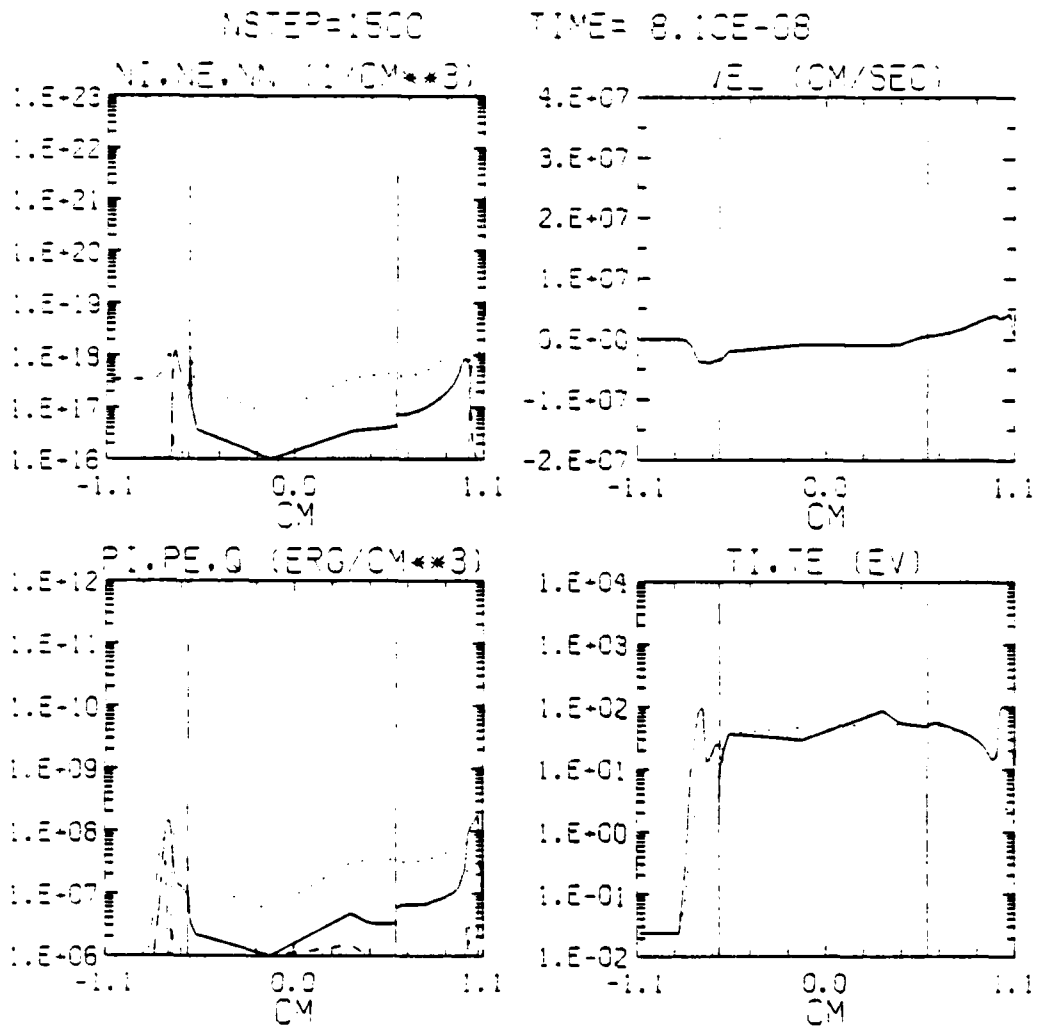


Figure 4g. Same as Fig. 4e except at the simulation time 81.0 nsec.

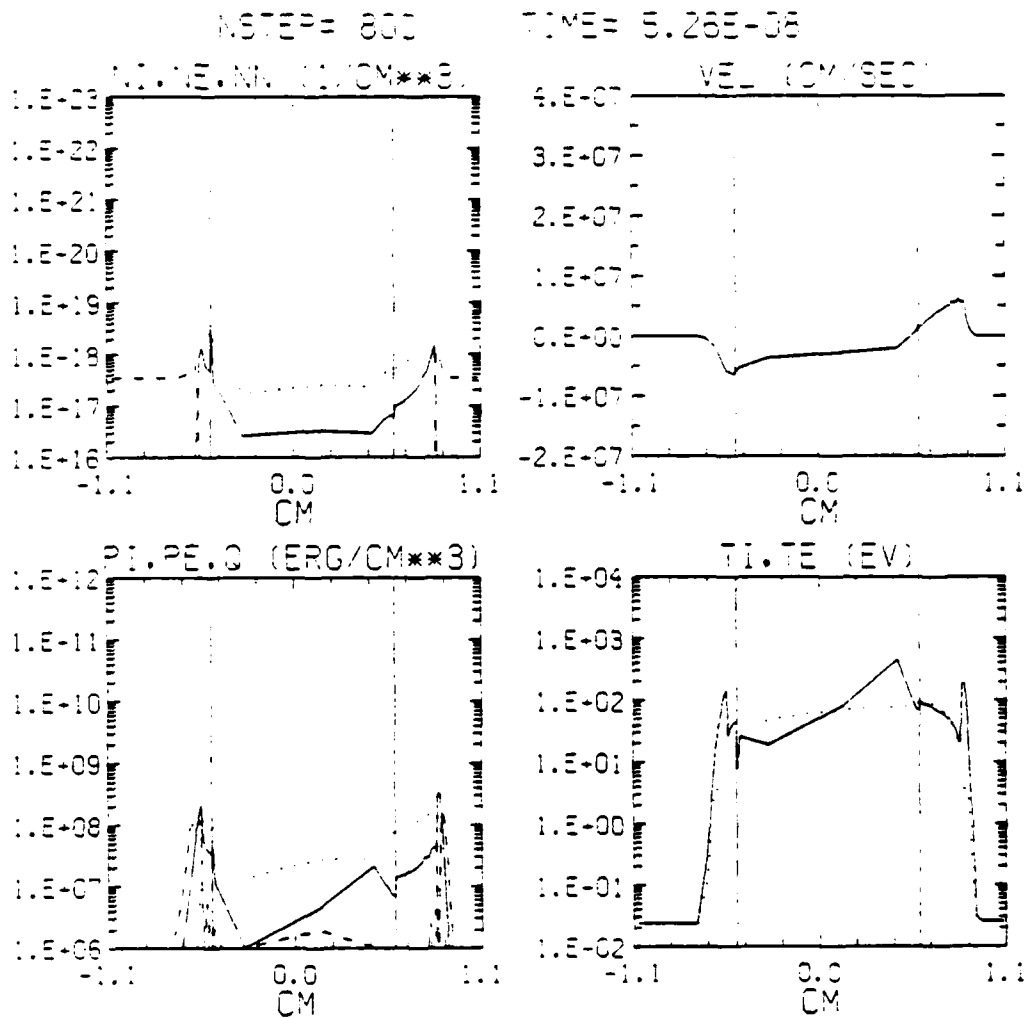


Figure 5a. Number density (NI = ions, NE = electrons, NN = neutrals), mass velocity, pressure (PI = ions, PE = electrons, Q = artificial viscosity) and temperature (TI = ions, TE = electrons) for model B at the simulation time 52.6 nsec.

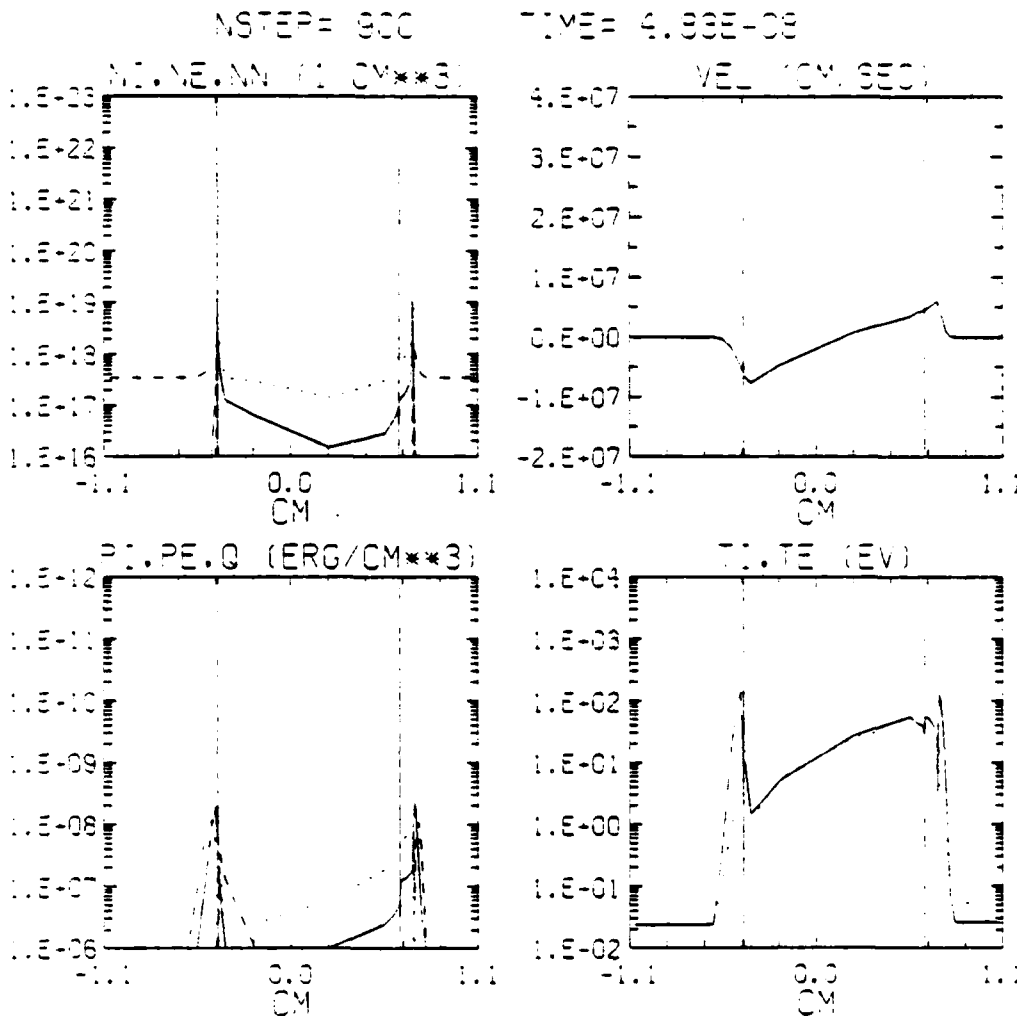


Figure 5b. Same as Fig. 5a except for model C at the simulation time 48.3 nsec.

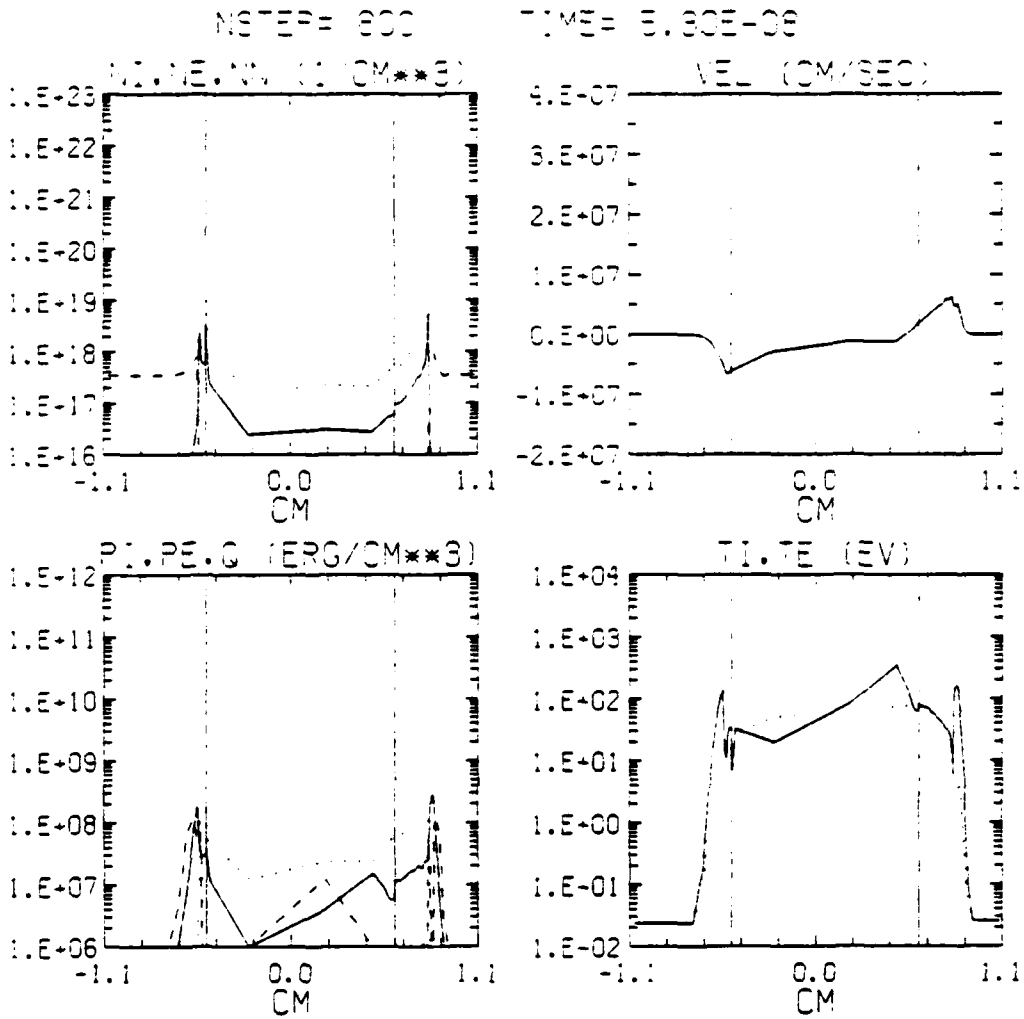


Figure 5c. Same as Fig. 5a except for model D at the simulation time 53.0 nsec.

# RAYLEIGH-TAYLOR GROWTH RATE

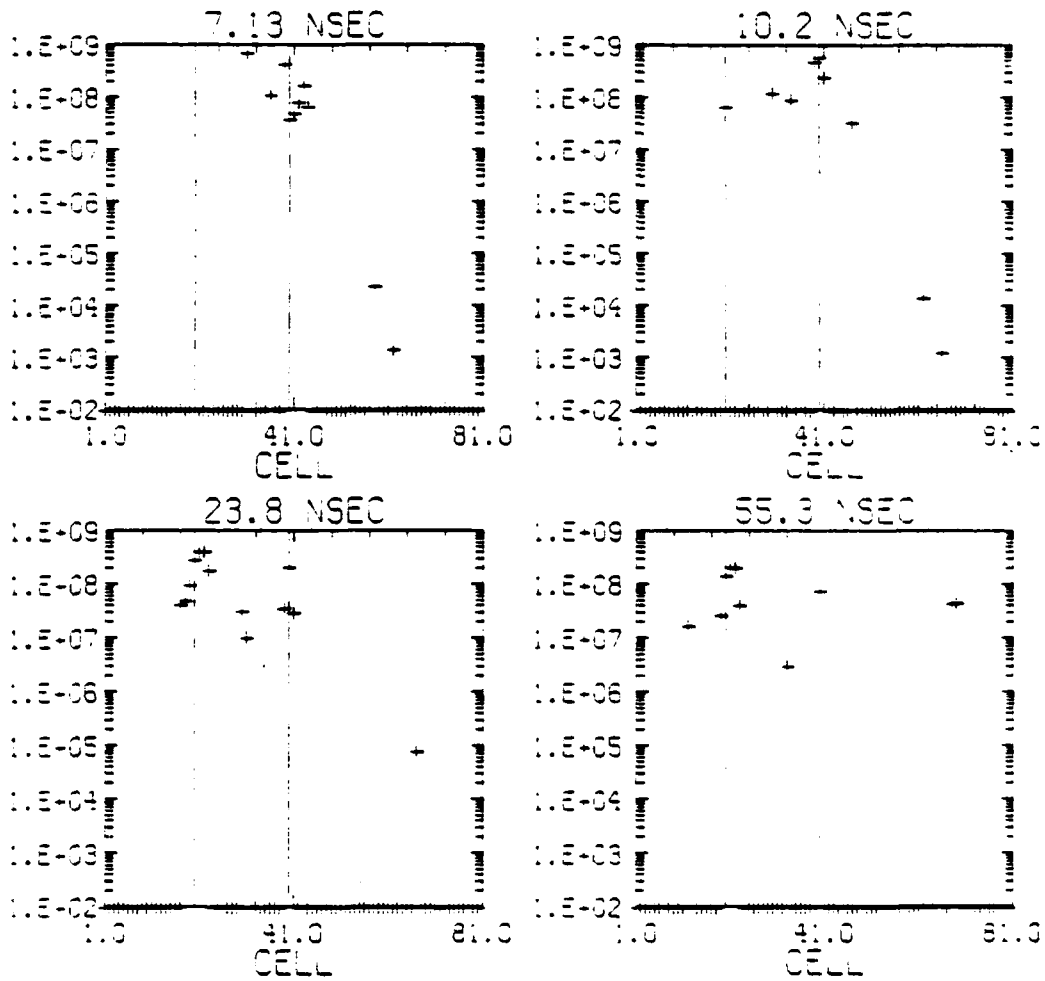


Figure 6. Growth rate in  $\text{nsec}^{-1}$  for the deceleration Rayleigh-Taylor instability at four times for the standard model. The rates are calculated from eqn.(32) of the text.

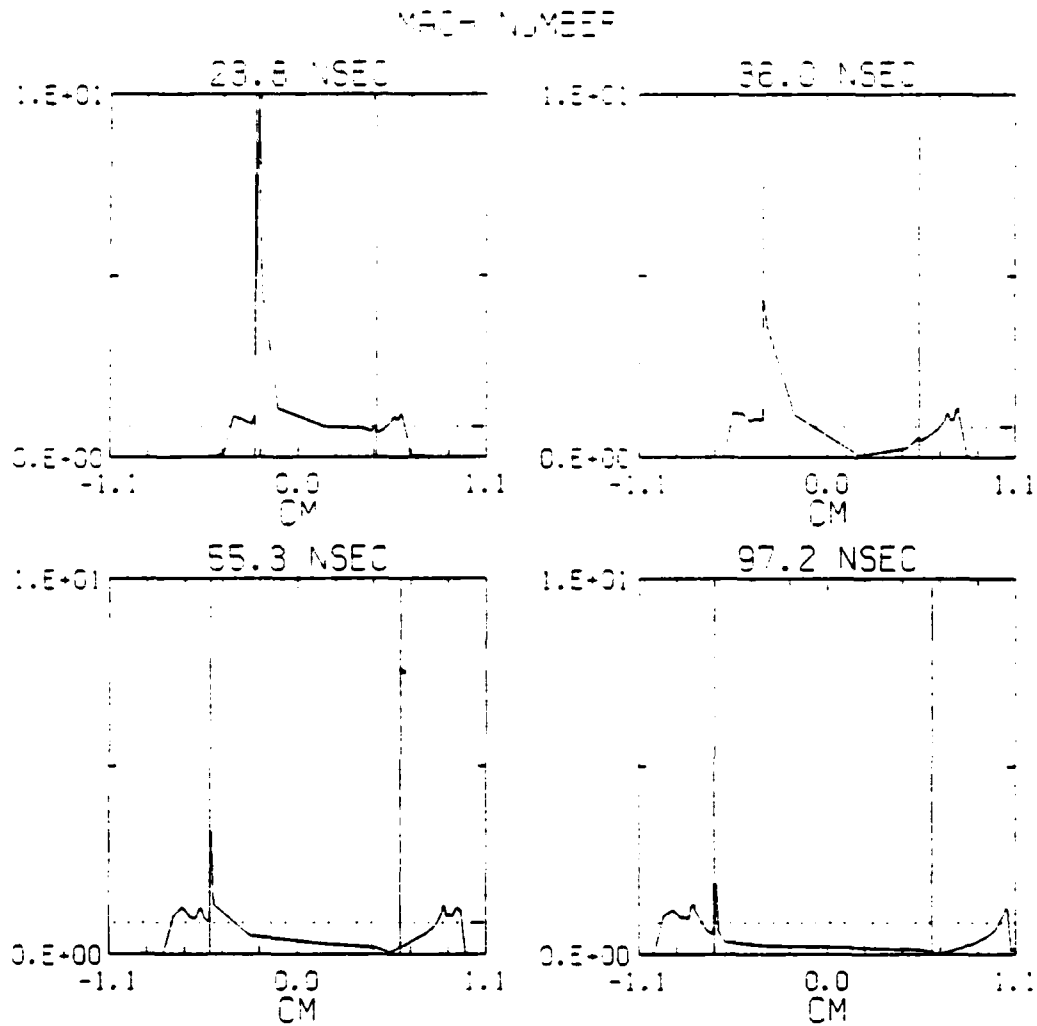


Figure 7. The local adiabatic ( $\gamma = 5/3$ ) Mach number as a function of position for four different times in the standard model. The horizontal dashed line is at the value unity.

## REFERENCES

1. B. H. Ripin, J. Grun, S. Kacenjar, E. A. McLean, and J. A. Stamper, NRL Memo Report #5268, "Introduction to the Laser-Hane Experiment and Summary of Low Pressure Interaction Results," (1984). (AD-A138 945)
2. J. A. Stamper, B. H. Ripin, and S. P. Oberschain, NRL Memo Report #5278, "Optical Imaging of a Coupling Region Between Interstreaming Plasma," (1984). (AD-A139 191)
3. B. H. Ripin, J. A. Stamper, and E. A. McLean, NRL Memo Report #5279, "Blast Wave Analysis of High Pressure Coupling Shells," (1984). (1984). (AD-A139 687)
4. S. I. Braginskii, "Transport Processes in A Plasma", in Reviews of Plasma Physics, Vol. I, ed. M. A. Leontovich, (Consultants Bureau: New York, 1965), p.205.
5. W. F. Noh, "Artificial Viscosity(Q) and Artificial Heat Flux(H) Errors for Spherically Divergent Shocks", Lawrence Livermore National Laboratory, Livermore, CA, UCRL-89623 (1983).
6. K. Hain, NRL Memo Report #3954, "ARIS Manual", (1979). (AD-A067 830)
7. R. F. Stellingwerf, DNA-TR-84-174, "Laser Target Design Scaling for the Upgraded NRL Facility", (1984). (AD-A156 030)
8. G. Arfken, Mathematical Methods for Physicists, (Academic Press: New York), p. 107.
9. R. C. Malone, R. L. McCrory, and R. L. Morse, Phys. Rev. Letters, 34, 721, (1975).
10. L. Spitzer, Jr. Physics of Fully Ionized Gases, (Interscience: New York, 1963), p.143.

11. W. M. Manheimer, Phys. of Fluids, 20, 265, "Energy Flux Limitation by Ion Acoustic Turbulence in Laser Fusion Schemes", (1977).
12. D. F. Smith and C. G. Lilliequist, Astrophys. J., 232, 582, "Confinement of Hot, Hard X-Ray Producing Electrons in Solar Flares", (1979).
13. J. F. Luciani, P. Mora, and J. Virmont, Phys. Rev. Letters, 51, 1664, "Nonlocal Heat Transport Due to Steep Temperature Gradients", (1983).
14. S. L. Thompson and H. S. Lauson, Sandia Laboratories Report SC-RR-71 0714, "Improvements in the Chart D Radiation-Hydrodynamic Code III: Revised Analytic Equations of State", (1979).
15. R. F. Schmalz and J. Meyer-ter-Vehn, Phys. of Fluids, 28, 932, "Equation of State Effects on Laser Accelerated Foils", (1985).
16. D. Duston, R. W. Clark, J. Davis, and J. P. Apruzese, Phys. Rev. A., 27, 1441, "Radiation Energetics of a Laser-Produced Plasma", (1983).
17. E. Hyman, M. Mulbrandon, and J. D. Huba, NRL Memo Report #5146, "Preliminary Report on UVDEP and PRODEP Results for the Laser/HANE Experiment", (1983). (AD-A132 110)
18. J. Stamper, B. H. Ripin, E. A. McLean, C. K. Manka, and A. N. Mostovych, reported at the "Early-Time High-Altitude Working Group Meeting", held at NRL, November, 1984.
19. J. Stamper, reported at the "Early-Time High-Altitude Working Group Meeting", held at NRL, May, 1985.
20. A. Solinger, S. Rappaport, and J. Buff, Astrophys. J., 201, 381, "Isothermal Blast Wave Model of Supernova Remnants," (1975).
21. J. L. Giuliani, NRL Memo Report #5671, "Obstacles as Probes of the Blast Wave Interior in the NRL Laser/HANE Simulation Experiment", 1985. (AD-A162 535)
22. R. F. Stellingwerf, C. L. Longmire, and R. E. Peterkin, AMRC-R-700, "Models of Early Time Hane Phenomena", (1985).

23. C. K. Manka and E. A. McLean, reported at the "Early-Time High-Altitude Working Group Meeting," held at NRL, May, 1985.
24. C. Jordan, Monthly Notices Royal Astro. Soc., 142, 501, "The Ionization Equilibrium of Elements between Carbon and Nickel", (1969).
25. D. G. Colombant, K. G. Whitney, D. A. Tidman, N. K. Winsor, J. Davis, Phys. Fluids, 18, 1687, "Laser Target Model", (1975).
26. J. U. Brackbill and S. R. Goldman, Comm. Pure and Applied Math, 36, 415, "Magnetohydrodynamics in Laser Fusion: Fluid Modeling of Energy Transport in Laser Targets", (1983).
27. G. J. Pert, J. Comp. Phys., 43, 111, "Algorithms for the Self-Consistent Generation of Magnetic Fields in Plasmas", (1981).

DISTRIBUTION LIST

DEPARTMENT OF DEFENSE

ASSISTANT SECRETARY OF DEFENSE  
COMM, CMD, CONT 7 INTELL  
WASHINGTON, DC 20301

DIRECTOR  
COMMAND CONTROL TECHNICAL CENTER  
PENTAGON RM BE 685  
WASHINGTON, DC 20301  
01CY ATTN C-650  
01CY ATTN C-312 R. MASON

DIRECTOR  
DEFENSE ADVANCED RSCH PROJ AGENCY  
ARCHITECT BUILDING  
1400 WILSON BLVD.  
ARLINGTON, VA 22209  
01CY ATTN NUCLEAR  
MONITORING RESEARCH  
01CY ATTN STRATEGIC TECH OFFICE

DEFENSE COMMUNICATION ENGINEER CENTER  
1860 WIEHLE AVENUE  
RESTON, VA 22090  
01CY ATTN CODE R410  
01CY ATTN CODE R812

DIRECTOR  
DEFENSE NUCLEAR AGENCY  
WASHINGTON, DC 20305  
01CY ATTN STVL  
04CY ATTN TITL  
01CY ATTN DDST  
03CY ATTN RAAE

COMMANDER  
FIELD COMMAND  
DEFENSE NUCLEAR AGENCY  
KIRTLAND, AFB, NM 87115  
01CY ATTN FOPR

DEFENSE NUCLEAR AGENCY  
SAO/DNA  
BUILDING 20676  
KIRTLAND AFB, NM 87115  
01CY D.C. THORNBURG

DIRECTOR  
INTERSERVICE NUCLEAR WEAPONS SCHOOL  
KIRTLAND AFB, NM 87115  
01CY ATTN DOCUMENT CONTROL

JOINT PROGRAM MANAGEMENT OFFICE  
WASHINGTON, DC 20330  
01CY ATTN J-3 WWMCCS EVALUATION  
OFFICE

DIRECTOR  
JOINT STRAT TGT PLANNING STAFF  
OFFUTT AFB  
OMAHA, NB 68113  
01CY ATTN JSTPS/JLKS  
01CY ATTN JPST G. GOETZ

CHIEF  
LIVERMORE DIVISION FLD COMMAND DNA  
DEPARTMENT OF DEFENSE  
LAWRENCE LIVERMORE LABORATORY  
P.O. BOX 808  
LIVERMORE, CA 94550  
01CY ATTN FCPRL

COMMANDANT  
NATO SCHOOL (SHAPE)  
APO NEW YORK 09172  
01CY ATTN U.S. DOCUMENTS OFFICER

UNDER SECY OF DEF FOR RSCH & ENGRG  
DEPARTMENT OF DEFENSE  
WASHINGTON, DC 20301  
01CY ATTN STRATEGIC & SPACE  
SYSTEMS (OS)

COMMANDER/DIRECTOR  
ATMOSPHERIC SCIENCES LABORATORY  
U.S. ARMY ELECTRONICS COMMAND  
WHITE SANDS MISSILE RANGE, NM 88002  
01CY ATTN DELAS-EC, F. NOLES

DIRECTOR  
BMD ADVANCED TECH CTR  
HUNTSVILLE OFFICE  
P.O. BOX 1500  
HUNTSVILLE, AL 35807  
01CY ATTN ATC-T MELVIN T. CAPPS  
01CY ATTN ATC-O W. DAVIES  
01CY ATTN ATC-R DON RUSS

PROGRAM MANAGER  
BMD PROGRAM OFFICE  
5001 EISENHOWER AVENUE  
ALEXANDRIA, VA 22333  
01CY ATTN DACS-BMT J. SHEA

CHIEF C-E- SERVICES DIVISION  
U.S. ARMY COMMUNICATIONS CMD  
PENTAGON RM 13269  
WASHINGTON, DC 20310  
01CY ATTN C- E-SERVICES DIVISION

COMMANDER  
FRADCOM TECHNICAL SUPPORT ACTIVITY  
DEPARTMENT OF THE ARMY  
FORT MONMOUTH, N.J. 07703  
01CY ATTN DRSEL-NL-RD H. BENNET  
01CY ATTN DRSEL-PL-ENV H. BOMKE  
01CY ATTN J.E. QUIGLEY

COMMANDER  
U.S. ARMY COMM-ELEC ENGRG INSTAL AGY  
FT. HUACHUCA, AZ 85613  
01CY ATTN CCC-EMEO GEORGE LANE

COMMANDER  
U.S. ARMY FOREIGN SCIENCE & TECH CTR  
220 7TH STREET, NE  
CHARLOTTESVILLE, VA 22901  
01CY ATTN DRXST-SD

COMMANDER  
U.S. ARMY MATERIAL DEV & READINESS CMD  
5001 EISENHOWER AVENUE  
ALEXANDRIA, VA 22333  
01CY ATTN DRCLDC J.A. BENDER

COMMANDER  
U.S. ARMY NUCLEAR AND CHEMICAL AGENCY  
7500 BACKLICK ROAD  
BLDG 2073  
SPRINGFIELD, VA 22150  
01CY ATTN LIBRARY

DIRECTOR  
U.S. ARMY BALLISTIC RESEARCH  
LABORATORY  
ABERDEEN PROVING GROUND, MD 21005  
01CY ATTN TECH LIBRARY,  
EDWARD BAICY

COMMANDER  
U.S. ARMY SATCOM AGENCY  
FT. MONMOUTH, NJ 07703  
01CY ATTN DOCUMENT CONTROL

COMMANDER  
U.S. ARMY MISSILE INTELLIGENCE AGENCY  
REDSTONE ARSENAL, AL 35809  
01CY ATTN JIM GAMBLE

DIRECTOR  
U.S. ARMY TRADOC SYSTEMS ANALYSIS  
ACTIVITY  
WHITE SANDS MISSILE RANGE, NM 88002  
01CY ATTN ATAA-SA  
01CY ATTN TCC/F. PAYAN JR.  
01CY ATTN ATTA-TAC LTC J. HESSE

COMMANDER  
NAVAL ELECTRONIC SYSTEMS COMMAND  
WASHINGTON, DC 20360  
01CY ATTN NAVALEX 034 T. HUGHES  
01CY ATTN PME 117  
01CY ATTN PME 117-T  
01CY ATTN CODE 5011

COMMANDING OFFICER  
NAVAL INTELLIGENCE SUPPORT CTR  
4301 SUITLAND ROAD, BLDG. 5  
WASHINGTON, DC 20390  
01CY ATTN MR. DUBBIN STIC 12  
01CY ATTN NISC-50  
01CY ATTN CODE 5404 J. GALET

COMMANDER  
NAVAL OCEAN SYSTEMS CENTER  
SAN DIEGO, CA 92152  
01CY ATTN J. FERGUSON

NAVAL RESEARCH LABORATORY  
WASHINGTON, DC 20375  
01CY ATTN CODE 4700 S.L. Ossakow,  
26 CYS IF UNCLASS  
(01CY IF CLASS)  
ATTN CODE 4780 J.D. HUBA, 50  
CYS IF UNCLASS, 01CY IF CLASS  
01CY ATTN CODE 4701 I. VITKOVITSKY  
01CY ATTN CODE 7500  
01CY ATTN CODE 7550  
01CY ATTN CODE 7580  
01CY ATTN CODE 7551  
01CY ATTN CODE 7555  
01CY ATTN CODE 4730 E. MCLEAN  
01CY ATTN CODE 4108  
01CY ATTN CODE 4730 B. RIPIN  
20CY ATTN CODE 2628

COMMANDER  
NAVAL SPACE SURVEILLANCE SYSTEM  
DAHLGREN, VA 22448  
01CY ATTN CAPT J.H. BURTON

OFFICER-IN-CHARGE  
NAVAL SURFACE WEAPONS CENTER  
WHITE OAK, SILVER SPRING, MD 20910  
01CY ATTN CODE F31

DIRECTOR  
STRATEGIC SYSTEMS PROJECT OFFICE  
DEPARTMENT OF THE NAVY  
WASHINGTON, DC 20376  
01CY ATTN NSP-2141  
01CY ATTN NSSP-2722 FRED WIMBERLY

COMMANDER  
NAVAL SURFACE WEAPONS CENTER  
DAHLGREN LABORATORY  
DAHLGREN, VA 22448  
01CY ATTN CODE DF-14 R. BUTLER

OFFICER OF NAVAL RESEARCH  
ARLINGTON, VA 22217  
01CY ATTN CODE 465  
01CY ATTN CODE 461  
01CY ATTN CODE 402  
01CY ATTN CODE 420  
01CY ATTN CODE 421

COMMANDER  
AEROSPACE DEFENSE COMMAND/DC  
DEPARTMENT OF THE AIR FORCE  
ENT AFB, CO 80912  
01CY ATTN DC MR. LONG

COMMANDER  
AEROSPACE DEFENSE COMMAND/XPD  
DEPARTMENT OF THE AIR FORCE  
ENT AFB, CO 80912  
01CY ATTN XPDQQ  
01CY ATTN XP

AIR FORCE GEOPHYSICS LABORATORY  
HANSCOM AFB, MA 01731  
01CY ATTN OPR HAROLD GARDNER  
01CY ATTN LKE  
KENNETH S.W. CHAMPION  
01CY ATTN OPR ALVA T. STAIR  
01CY ATTN PHD JURGEN BUCHAU  
01CY ATTN PHD JOHN P. MULLEN

AF WEAPONS LABORATORY  
KIRTLAND AFT, NM 87117  
01CY ATTN SUL  
01CY ATTN CA ARTHUR H. GUENTHER  
01CY ATTN NTYCE 1LT. G. KRAJEI

AFTAC  
PATRICK AFB, FL 32925  
01CY ATTN TN

AIR FORCE AVIONICS LABORATORY  
WRIGHT-PATTERSON AFB, OH 45433  
01CY ATTN AAD WADE HUNT  
01CY ATTN AAD ALLEN JOHNSON

DEPUTY CHIEF OF STAFF  
RESEARCH, DEVELOPMENT, & ACQ  
DEPARTMENT OF THE AIR FORCE  
WASHINGTON, DC 20330  
01CY ATTN AFRDQ

HEADQUARTERS  
ELECTRONIC SYSTEMS DIVISION  
DEPARTMENT OF THE AIR FORCE  
HANSCOM AFB, MA 01731-5000  
01CY ATTN J. DEAS  
ESD/SCD-4

COMMANDER  
FOREIGN TECHNOLOGY DIVISION, AFSC  
WRIGHT-PATTERSON AFB, OH 45433  
01CY ATTN NICD LIBRARY  
01CY ATTN ETDP B. BALLARD

COMMANDER  
ROME AIR DEVELOPMENT CENTER, AFSC  
GRIFFISS AFB, NY 13441  
01CY ATTN DOC LIBRARY/TSLD  
01CY ATTN OCSE V. COYNE

STRATEGIC AIR COMMAND/XPFS  
OFFUTT AFB, NB 68113  
01CY ATTN ADWATE MAJ BRUCE BAUER  
01CY ATTN NRT  
01CY ATTN DOK CHIEF SCIENTIST

SAMSO/SK  
P.O. BOX 92960  
WORLDWAY POSTAL CENTER  
LOS ANGELES, CA 90009  
01CY ATTN SKA (SPACE COMM SYSTEMS)  
M. CLAVIN

SAMSO/MN  
NORTON AFB, CA 92409  
(MINUTEMAN)  
01CY ATTN MNNL

COMMANDER  
ROME AIR DEVELOPMENT CENTER, AFSC  
HANSCOM AFB, MA 01731  
01CY ATTN SEP A. LORENTZEN

DEPARTMENT OF ENERGY  
LIBRARY ROOM G-042  
WASHINGTON, DC 20545  
01CY ATTN DOC CON FOR A. LABOWITZ

DEPARTMENT OF ENERGY  
ALBUQUERQUE OPERATIONS OFFICE  
P.O. BOX 5400  
ALBUQUERQUE, NM 87115  
01CY ATTN DOC CON FOR D. SHERWOOD

EG&G, INC.  
LOS ALAMOS DIVISION  
P.O. BOX 809  
LOS ALAMOS, NM 85544  
01CY ATTN DOC CON FOR J. BREEDLOVE

UNIVERSITY OF CALIFORNIA  
LAWRENCE LIVERMORE LABORATORY  
P.O. BOX 808  
LIVERMORE, CA 94550  
01CY ATTN DOC CON FOR TECH INFO  
DEPT  
01CY ATTN DOC CON FOR L-389 R. OTT  
01CY ATTN DOC CON FOR L-31 R. HAGER

LOS ALAMOS NATIONAL LABORATORY  
P.O. BOX 1663  
LOS ALAMOS, NM 87545  
01CY ATTN DOC CON FOR J. WOLCOTT  
01CY ATTN DOC CON FOR R.F. TASCHEK  
01CY ATTN DOC CON FOR E. JONES  
01CY ATTN DOC CON FOR J. MALIK  
01CY ATTN DOC CON FOR R. JEFFRIES  
01CY ATTN DOC CON FOR J. ZINN  
01CY ATTN DOC CON FOR D. WESTERVELT  
01CY ATTN D. SAPPENFIELD

LOS ALAMOS NATIONAL LABORATORY  
MS D438  
LOS ALAMOS, NM 87545  
01CY ATTN S.P. GARY  
01CY ATTN J. BOROVSKY

SANDIA LABORATORIES  
P.O. BOX 5800  
ALBUQUERQUE, NM 87115  
01CY ATTN DOC CON FOR W. BROWN  
01CY ATTN DOC CON FOR A.  
THORNBROUGH  
01CY ATTN DOC CON FOR T. WRIGHT  
01CY ATTN DOC CON FOR D. DAHLGREN  
01CY ATTN DOC CON FOR 3141  
01CY ATTN DOC CON FOR SPACE PROJECT  
DIV

SANDIA LABORATORIES  
LIVERMORE LABORATORY  
P.O. BOX 969  
LIVERMORE, CA 94550  
01CY ATTN DOC CON FOR B. MURPHEY  
01CY ATTN DOC CON FOR T. COOK

OFFICE OF MILITARY APPLICATION  
DEPARTMENT OF ENERGY  
WASHINGTON, DC 20545  
01CY ATTN DOC CON DR. YO SONG

OTHER GOVERNMENT

INSTITUTE FOR TELECOM SCIENCES  
NATIONAL TELECOMMUNICATIONS & INFO  
ADMIN  
BOULDER, CO 80303  
01CY ATTN L. BERRY

NATIONAL OCEANIC & ATMOSPHERIC ADMIN  
ENVIRONMENTAL RESEARCH LABORATORIES  
DEPARTMENT OF COMMERCE  
BOULDER, CO 80302  
01CY ATTN R. GRUBB  
01CY ATTN AERONOMY LAB G. REID

DEPARTMENT OF DEFENSE CONTRACTORS

AEROSPACE CORPORATION  
P.O. BOX 92957  
LOS ANGELES, CA 90009  
01CY ATTN I. GARFUNKEL  
01CY ATTN T. SALMI  
01CY ATTN V. JOSEPHSON  
01CY ATTN S. BOWER  
01CY ATTN D. OLSEN

ANALYTICAL SYSTEMS ENGINEERING CORP  
5 OLD CONCORD ROAD  
BURLINGTON, MA 01803  
01CY ATTN RADIO SCIENCES

AUSTIN RESEARCH ASSOC., INC.  
1901 RUTLAND DRIVE  
AUSTIN, TX 78758  
01CY ATTN L. SLOAN  
01CY ATTN R. THOMPSON

BERKELEY RESEARCH ASSOCIATES, INC.  
P.O. BOX 983  
BERKELEY, CA 94701  
01CY ATTN J. WORKMAN  
01CY ATTN C. PRETTIE  
01CY ATTN S. BRECHT

BOEING COMPANY, THE  
P.O. BOX 3707  
SEATTLE, WA 98124  
01CY ATTN G. KEISTER  
01CY ATTN D. MURRAY  
01CY ATTN G. HALL  
01CY ATTN J. KENNEY

CHARLES STARK DRAPER LABORATORY, INC.  
555 TECHNOLOGY SQUARE  
CAMBRIDGE, MA 02139  
01CY ATTN D.B. COX  
01CY ATTN J.P. GILMORE

COMSAT LABORATORIES  
LINTHICUM ROAD  
CLARKSBURG, MD 20734  
01CY ATTN G. HYDE

CORNELL UNIVERSITY  
DEPARTMENT OF ELECTRICAL ENGINEERING  
ITHACA, NY 14850  
01CY ATTN D.T. FARLEY, JR.

ELECTROSPACE SYSTEMS, INC.  
BOX 1359  
RICHARDSON, TX 75080  
01CY ATTN H. LOGSTON  
01CY ATTN SECURITY (PAUL PHILLIPS)

EOS TECHNOLOGIES, INC.  
606 Wilshire Blvd.  
Santa Monica, CA 90401  
01CY ATTN C.B. GABBARD  
01CY ATTN R. LELEVIER

ESL, INC.  
495 JAVA DRIVE  
SUNNYVALE, CA 94086  
01CY ATTN J. ROBERTS  
01CY ATTN JAMES MARSHALL

GENERAL ELECTRIC COMPANY  
SPACE DIVISION  
VALLEY FORGE SPACE CENTER  
GODDARD BLVD KING OF PRUSSIA  
P.O. BOX 8555  
PHILADELPHIA, PA 19101  
01CY ATTN M.H. BORTNER  
SPACE SCI LAB

GENERAL ELECTRIC TECH SERVICES  
CO., INC.  
HMES  
COURT STREET  
SYRACUSE, NY 13201  
01CY ATTN G. MILLMAN

GEOPHYSICAL INSTITUTE  
UNIVERSITY OF ALASKA  
FAIRBANKS, AK 99701  
(ALL CLASS ATTN: SECURITY OFFICER)  
01CY ATTN T.N. DAVIS (UNCLASS ONLY)  
01CY ATTN TECHNICAL LIBRARY  
01CY ATTN NEAL BROWN (UNCLASS ONLY)

GTE SYLVANIA, INC.  
ELECTRONICS SYSTEMS GRP-EASTERN DIV  
77 A STREET  
NEEDHAM, MA 02194  
01CY ATTN DICK STEINHOF

HSS, INC.  
2 ALFRED CIRCLE  
BEDFORD, MA 01730  
01CY ATTN DONALD HANSEN

ILLINOIS, UNIVERSITY OF  
107 COBLE HALL  
150 DAVENPORT HOUSE  
CHAMPAIGN, IL 61820  
(ALL CORRES ATTN DAN MCCLELLAND)  
01CY ATTN K. YEH

INSTITUTE FOR DEFENSE ANALYSES  
1801 NO. BEAUREGARD STREET  
ALEXANDRIA, VA 22311  
01CY ATTN J.M. AFIN  
01CY ATTN ERNEST BAUER  
01CY ATTN HANS WOLFARD  
01CY ATTN JOEL BENGSTON

INTL TEL & TELEGRAPH CORPORATION  
500 WASHINGTON AVENUE  
NUTLEY, NJ 07110  
01CY ATTN TECHNICAL LIBRARY

JAYCOR  
1011 TORREYANA ROAD  
P.O. BOX 35154  
SAN DIEGO, CA 92133  
01CY ATTN J.L. SPERLING

JOHNS HOPKINS UNIVERSITY  
APPLIED PHYSICS LABORATORY  
JOHNS HOPKINS ROAD  
LAUREL, MD 20810  
01CY ATTN DOCUMENT LIBRARIAN  
01CY ATTN THOMAS POTEIRA  
01CY ATTN JOHN DASSOULAS

KAMAN SCIENCES CORP  
P.O. BOX 7463  
COLORADO SPRINGS, CO 80933  
01CY ATTN T. MEAGHER

KAMAN TEMPO-CENTER FOR ADVANCED  
STUDIES  
816 STATE STREET (P.O DRAWER QQ)  
SANTA BARBARA, CA 93102  
01CY ATTN DASIAC  
01CY ATTN WARREN S. KNAPP  
01CY ATTN WILLIAM MCNAMARA  
01CY ATTN B. GAMBILL

LINKABIT CORP  
10453 ROSELLE  
SAN DIEGO, CA 92121  
01CY ATTN IRWIN JACOBS

LOCKHEED MISSILES & SPACE CO., INC  
P.O. BOX 504  
SUNNYVALE, CA 94088  
01CY ATTN DEPT 60-12  
01CY ATTN D.R. CHURCHILL

LOCKHEED MISSILES & SPACE CO., INC.  
3251 HANOVER STREET  
PALO ALTO, CA 94304  
01CY ATTN MARTIN WALT DEPT 52-12  
01CY ATTN W.L. IMHOF DEPT 52-12  
01CY ATTN RICHARD G. JOHNSON  
DEPT 52-12  
01CY ATTN J.B. CLADIS DEPT 52-12

MARTIN MARIETTA CORP  
ORLANDO DIVISION  
P.O. BOX 5837  
ORLANDO, FL 32805  
01CY ATTN R. HEFFNER

MCDONNELL DOUGLAS CORPORATION  
5301 BOLSA AVENUE  
HUNTINGTON BEACH, CA 92647  
01CY ATTN N. HARRIS  
01CY ATTN J. MOULE  
01CY ATTN GEORGE MROZ  
01CY ATTN W. OLSON  
01CY ATTN R.W. HALPRIN  
01CY ATTN TECHNICAL  
LIBRARY SERVICES

MISSION RESEARCH CORPORATION  
735 STATE STREET  
SANTA BARBARA, CA 93101  
01CY ATTN P. FISCHER  
01CY ATTN W.F. CREVIER  
01CY ATTN STEVEN L. GUTSCHE  
01CY ATTN R. BOGUSCH  
01CY ATTN R. HENDRICK  
01CY ATTN RALPH KILB  
01CY ATTN DAVE SOWLE  
01CY ATTN F. FAJEN  
01CY ATTN M. SCHEIBE  
01CY ATTN CONRAD L. LONGMIRE  
01CY ATTN B. WHITE  
01CY ATTN R. STAGAT

MISSION RESEARCH CORP.  
1720 RANDOLPH ROAD, S.E.  
ALBUQUERQUE, NM 87106  
01CY R. STELLINGWERF  
01CY M. ALME  
01CY L. WRIGHT

MITRE CORP  
WESTGATE RESEARCH PARK  
1820 DOLLY MADISON BLVD  
MCLEAN, VA 22101  
01CY ATTN W. HALL  
01CY ATTN W. FOSTER

PACIFIC-SIERRA RESEARCH CORP  
12340 SANTA MONICA BLVD.  
LOS ANGELES, CA 90025  
01CY ATTN E.C. FIELD, JR.

PENNSYLVANIA STATE UNIVERSITY  
IONOSPHERE RESEARCH LAB  
318 ELECTRICAL ENGINEERING EAST  
UNIVERSITY PARK, PA 16802  
(NO CLASS TO THIS ADDRESS)  
01CY ATTN IONOSPHERIC RESEARCH LAB

PHOTOMETRICS, INC.  
4 ARROW DRIVE  
WOBURN, MA 01801  
01CY ATTN IRVING L. KOFSKY

PHYSICAL DYNAMICS, INC.  
P.O. BOX 3027  
BELLEVUE, WA 98009  
01CY ATTN E.J. FREMOUW

PHYSICAL DYNAMICS, INC.  
P.O. BOX 10367  
OAKLAND, CA 94610  
ATTN A. THOMSON  
  
R & D ASSOCIATES  
P.O. BOX 9695  
MARINA DEL REY, CA 90291  
01CY ATTN FORREST GILMORE  
01CY ATTN WILLIAM B. WRIGHT, JR.  
01CY ATTN WILLIAM J. KARZAS  
01CY ATTN H. ORY  
01CY ATTN C. MACDONALD

RAND CORPORATION, THE  
15450 COHASSET STREET  
VAN NUYS, CA 91406  
01CY ATTN CULLEN CRAIN  
01CY ATTN ED BEDROZIAN

RAYTHEON CO.  
528 BOSTON POST ROAD  
SUDBURY, MA 01776  
01CY ATTN BARBARA ADAMS

RIVERSIDE RESEARCH INSTITUTE  
330 WEST 42nd STREET  
NEW YORK, NY 10036  
01CY ATTN VINCE TRAPANI

SCIENCE APPLICATIONS, INC.  
1150 PROSPECT PLAZA  
LA JOLLA, CA 92037  
01CY ATTN LEWIS M. LINSON  
01CY ATTN DANIEL A. HAMLIN  
01CY ATTN E. FRIEMAN  
01CY ATTN E.A. STRAKER  
01CY ATTN CURTIS A. SMITH

SCIENCE APPLICATIONS, INC  
1710 GOODRIDGE DR.  
MCLEAN, VA 22102  
01CY J. COCKAYNE  
01CY E. HYMAN

SRI INTERNATIONAL  
333 RAVENSWOOD AVENUE  
MENLO PARK, CA 94025

01CY ATTN J. CASPER  
01CY ATTN DONALD NEILSON  
01CY ATTN ALAN BURNS  
01CY ATTN G. SMITH  
01CY ATTN R. TSUNODA  
01CY ATTN DAVID A. JOHNSON  
01CY ATTN WALTER G. CHESNUT  
01CY ATTN CHARLES L. RINO  
01CY ATTN WALTER JAYE  
01CY ATTN J. VICKREY  
01CY ATTN RAY L. LEADABRAND  
01CY ATTN G. CARPENTER  
01CY ATTN G. PRICE  
01CY ATTN R. LIVINGSTON  
01CY ATTN V. GONZALES  
01CY ATTN D. MCDANIEL

TECHNOLOGY INTERNATIONAL CORP  
75 WIGGINS AVENUE  
BEDFORD, MA 01730  
01CY ATTN W.P. BOQUIST

TRW DEFENSE & SPACE SYS GROUP  
ONE SPACE PARK  
REDONDO BEACH, CA 90278  
01CY ATTN R. K. PLEBUCH  
01CY ATTN S. ALTSCHULER  
01CY ATTN D. DEE  
01CY ATTN D/ STOCKWELL  
SNTF/1575

VISIDYNE  
SOUTH BEDFORD STREET  
BURLINGTON, MA 01803  
01CY ATTN W. REIDY  
01CY ATTN J. CARPENTER  
01CY ATTN C. HUMPHREY

UNIVERSITY OF PITTSBURGH  
PITTSBURGH, PA 15213  
01CY ATTN: N. ZABUSKY

DIRECTOR OF RESEARCH  
U. S. NAVAL ACADEMY  
ANNAPOLIS, MD 21402  
02CY

CODE 1220  
01CY

END

FILMED

6-86

DITIC